

Ampli-Flection for 6G: Active-RIS-Aided Aerial Backhaul with Full 3D Coverage

Hong-Bae Jeon, *Member, IEEE*, and Chan-Byoung Chae, *Fellow, IEEE*

Abstract—In this paper, we propose a novel aerial backhaul architecture that employs an aerial active reconfigurable intelligent surface (RIS) to achieve energy-efficient, full 3D coverage including UAV-BSs and ground users in 6G wireless networks. Unlike prior aerial-RIS approaches limited to 2D coverage with only servicing ground users or passive operation, the proposed design integrates an active-RIS onto a high-altitude aerial platform, enabling reliable line-of-sight links and overcoming multiplicative fading through amplification. In a scenario with UAV-BSs deployed to handle sudden traffic surges in urban areas, the aerial-active-RIS both reflects and amplifies backhaul signals to overcome blockage. We jointly optimize the aerial platform placement, array partitioning, and RIS phase configuration to maximize UAV-BS energy-efficiency. Simulation results confirm that the proposed method significantly outperforms benchmarks, demonstrating its strong potential to deliver resilient backhaul connectivity with comprehensive 3D coverage in 6G networks.

Index Terms—Active reconfigurable intelligent surface, unmanned aerial vehicle, wireless backhaul, non-convex optimization, energy-efficiency.

I. INTRODUCTION

OF LATE, the rapid expansion of data-driven applications with the push for extended wireless coverage in beyond fifth-generation (5G) and sixth-generation (6G) networks have driven an unprecedented demand for providing ultra-reliable and high-capacity communications anywhere [2]–[4]. In response, researchers have been exploring the deployment of aerial base stations, realized through unmanned-aerial-vehicle-base-stations (UAV-BSs), for rapid and flexible coverage extensions [5], [6]. These UAV-BSs present a compelling solution for extending network coverage to areas where conventional base station infrastructure is inadequate, offering rapid deployment capabilities in emergency or high-traffic scenarios. Their high-altitude operation further enhances the likelihood of rich line-of-sight (LoS) links [7], [8], thereby improving communication reliability and efficiency. To enable efficient UAV-BS deployment, prior studies have investigated deployment strategy design [9], [10], trajectory optimization [11], [12], and power control schemes [13], [14]. One of the critical challenges that remains for deploying UAV-BSs is the backhaul connectivity, particularly in dense urban areas

This work was supported by Hankuk University of Foreign Studies Research Fund of 2026. This article was presented in part at the IEEE ICTC 2022, Jeju Island, South Korea, October 19-21, 2022 [1]. (*Corresponding Author: Chan-Byoung Chae*.)

H.-B. Jeon is with the Department of Information Communications Engineering, Hankuk University of Foreign Studies, Yong-in, 17035, Korea (e-mail: hongbae08@hufs.ac.kr).

C.-B. Chae is with the School of Integrated Technology, Yonsei University, Seoul 03722, Korea (e-mail: cbchae@yonsei.ac.kr).

where obstacles obstruct direct backhaul links from terrestrial sources and generates non-LoS (NLoS) components, which severely deteriorates the system’s energy-efficiency, posing a critical challenge for 6G wireless networks operating with higher spectrum [15]–[17].

Therefore, the reconfigurable intelligent surfaces (RIS) have been explored as a means to enhance wireless coverage and mitigate blockages [18]–[21]. RIS is an artificial metasurface composed of passive reflecting elements capable of adjusting both the amplitude and phase of an incident signal [22], [23]. Furthermore, due to its passive array architecture, the RIS exhibits high channel capacity with low power consumption, which leads to the energy-efficiency compared to conventional decode-and-forward or amplify-and-forward (DF/AF) relays in several scenarios [24]–[26]. However, conventional RIS has passive reflection elements, which highly suffer from severe “multiplicative fading,” where the path loss is given by the multiplication of Tx-to-RIS and RIS-to-Rx links, limiting their effectiveness in practical scenarios [27], [28]. These disadvantages become more severe when the RIS is deployed in terrestrial infrastructure on dense urban areas.

To overcome the fundamental physical limitation imposed by the multiplicative fading effect of cascaded channels in RIS-assisted systems, the concept of active-RIS has recently been proposed [27], [29]. Unlike conventional passive-RISs, which only reflect incident signals without amplification, active-RISs incorporate reflection-type amplifiers within each element, thereby enabling signal amplification at the cost of additional power consumption [30]. This capability fundamentally changes the power-rate trade-off and opens up new possibilities for performance enhancement in future 6G wireless networks.

Early studies, such as [27], focused on characterizing the performance gains of active-RIS over passive-RIS through sum-rate maximization and comparative analyses, demonstrating that active-RIS can effectively mitigate the double-fading loss inherent in passive architectures. These works established the potential of active-RIS as a promising technology for next-generation systems. Building upon this foundation, subsequent research addressed practical implementation challenges. In particular, [31] investigated a sub-connected active-RIS architecture and proposed a joint beamforming design that balances hardware complexity and performance, revealing important trade-offs between achievable gains and circuit-level constraints. From a performance perspective, [28], [32] further examined the SNR advantages of active-RIS under a unified power budget, showing that, when properly optimized, active-RIS can significantly outperform passive-RIS counterparts.

More recently after performance characterization and architectural investigations, attention has shifted toward robustness and practical deployability. To bridge the gap between theoretical analysis and real-world operation, [33], [34] studied active-RIS transmission designs under partial channel state information (CSI). Specifically, [33] aimed at maximizing the average sum-rate, while [34] focused on minimizing the average total transmit power subject to rate and outage probability constraints. These works highlight the importance of accounting for CSI uncertainty when designing active-RIS-assisted systems.

Most prior work, however, has primarily focused on deploying the active-RIS in terrestrial environments, such as those involving buildings and walls. These environments impose several limitations on communication performance. In dense urban areas with many buildings, reliable transmission often depends on multiple reflections, which requires deploying a large number of RIS units to alleviate severe signal attenuation. Moreover, a terrestrial RIS can only reflect signals from the source to destinations located on the same side, thereby restricting the angular range of reflection and preventing isotropic coverage over $0^\circ \sim 360^\circ$ arrival angles. Several studies have investigated the deployment of RIS on aerial platforms (e.g., [35]–[37]); however, most of these works focus on conventional passive RIS architectures and consider only 2D coverage, or assume fixed transmit power at the source, thereby largely overlooking energy-efficiency considerations. Although a few recent studies have explored active-RIS-assisted aerial systems [38]–[40], they still restrict their scope to 2D coverage scenarios¹, which limits their applicability in dense urban 6G environments with heterogeneous mobility and altitude-dependent service demands.

In contrast, this paper proposes a novel aerial active-RIS architecture that explicitly distinguishes the geometric benefits of aerial deployment from the amplification-enabled gains introduced by the active-RIS itself. While the elevated platform inherently improves LoS availability and alleviates blockage through favorable 3D geometry, the active-RIS provides an additional and fundamentally different advantage by amplifying the reflected signals at the element level. This amplification capability mitigates the multiplicative path-loss of cascaded source-RIS-destination links, which is an important issue due to the long link distance of aerial platform and cannot be achieved by aerial placement or passive RIS alone under the same power budget [41]. As a result, the proposed architecture enables energy-efficient 3D coverage and, for the first time, facilitates an aerial-active-RIS-assisted backhaul network capable of reliably supporting UAV-BSs and heterogeneous users in future 6G wireless networks.

The key contributions are summarized as follows:

- 1) We propose a novel aerial-active-RIS architecture aimed at enhancing 3D backhaul connectivity to UAV-BSs in urban environments characterized by severe blockages.

¹In this paper, we define “2D coverage” as the servicing of only ground users, whereas “3D coverage” refers to the service of both aerial and ground users, which constitutes a geometrical extension of 2D coverage. It is emphasized that the term “3D coverage” in this work refers to geometry-aware coverage over a three-dimensional spatial region, rather than full-dimensional beamforming enabled by planar arrays.

The proposed scheme deploys an RIS on a high-altitude platform, where each RIS element is equipped with an active amplifier, ensuring both a rich LoS component and robustness against multiplicative fading, respectively. To maximize the received SNR and minimize the transmit power, we show that the maximum-ratio transmission (MRT) strategy achieves the purpose.

- 2) We verify that equal amplification gain across active-RIS elements is a feasible approach for optimizing the energy-efficiency by minimizing the total consumed power of the system. Under this assumption, an optimization framework is developed to determine the placement, array-partitioning strategy, phase control and optimal amplification gain of the aerial-active-RIS with the objective of maximizing energy-efficiency. Specifically, a nonzero closed-form value of the source transmit power for each UAV-BS is derived, and a minimization problem is formulated by adjusting the numerator and denominator of the value. The problem is efficiently solved using the global criterion method, which selects a minimal-total-distance operating point corresponding to a Pareto-efficient solution, and considering the partition of full RIS array, respectively.
- 3) The proposed approach is evaluated numerically in a realistic urban outdoor environment with 10^3 randomly distributed ground users and corresponding UAV-BSs. Extensive numerical results demonstrate that the proposed aerial-active-RIS scheme significantly outperforms conventional benchmarks including the aerial-AF-relay and the aerial-passive-RIS schemes and aerial-active-RIS with randomly determined amplification gain in terms of energy-efficiency.

II. SYSTEM MODEL

A. Aerial Backhaul with Conventional Passive-RIS

We consider an urban area \mathcal{G} with origin $\rho_{\mathcal{G}}$ on xy-plane, as depicted in Fig. 1(a). We assume that \mathcal{G} contains N_0 ground users equipped with omnidirectional antenna, and served by multiple stationary UAV-BSs with a directional antenna, represented as $\mathbb{M} = \{1, \dots, M_0\}$. The directional antenna of each UAV-BS has different azimuth and elevation half-power beamwidths (HPBW) [42]. The 3D coordinates of a UAV-BS m are expressed as $\rho_m \triangleq [\mathbf{w}_m^T \ h_m]^T$, with its 2D coordinate \mathbf{w}_m and altitude h_m .

To alleviate interference among adjacent cells, we assume that each UAV-BS serves a distinct, non-overlapping subset of users. In this context, the Ellipse Clustering algorithm [8] is employed to allocate ground users and determine M_0 , while significantly reducing the transmit power through optimized 3D deployment. Under this setup, the throughput C_m of UAV-BS m is expressed as

$$C_m = \sum_{n \in \mathbb{U}_m} \frac{B_f}{|\mathbb{U}_m|} \log_2 \left(1 + \frac{P_{f,n}}{\sigma_f^2} \right), \quad (1)$$

where \mathbb{U}_m represents the user set served by UAV-BS m , B_f denotes the fronthaul bandwidth, which is evenly divided among the $|\mathbb{U}_m|$ users in \mathbb{U}_m , $P_{f,n}$ is the received power at

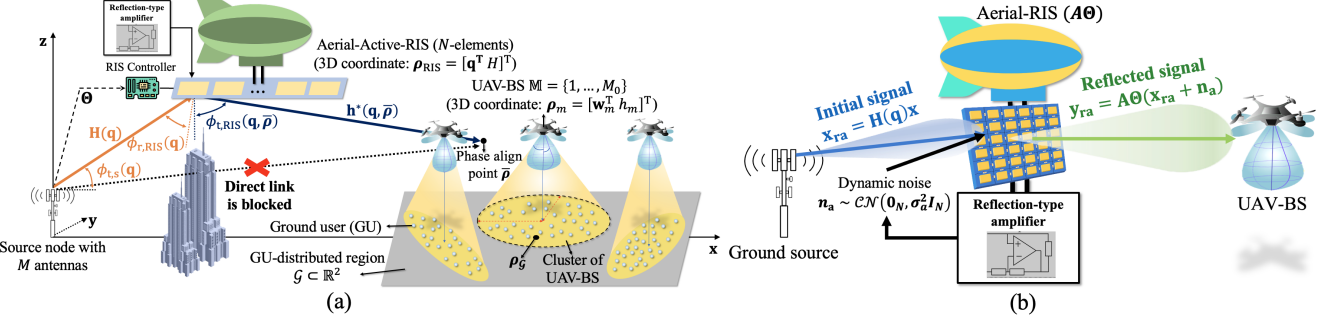


Fig. 1. (a) UAV-BS access network supported by an aerial-active-RIS backhaul and (b) signal model illustration of the aerial-active-RIS.

user $n \in \mathbb{U}_m$, and $\sigma_{f,m}^2$ represents the noise power of the fronthaul link for UAV-BS m . By adopting the frequency-division-multiple-access (FDMA) within each cell and non-overlapping UAV-BS coverage regions, both intra- and inter-cell interference are eliminated, and the achievable rate in (1) directly follows.

For an aerial-active-RIS which maintains an altitude H , and designating the first element as the reference, the 3D coordinates of the aerial-RIS are expressed as $\rho_{\text{RIS}} \triangleq [\mathbf{q}^T \mathbf{H}]^T$. We consider a source at origin, which is equipped with a uniform linear array (ULA) comprising M antennas with inter-element spacing d_s and an antenna gain of G_s . Note that although the source and the aerial-active-RIS employ ULAs, the considered coverage is inherently “three-dimensional”, as the RIS and UAV-BS location, propagation distance, and elevation angle are explicitly characterized in a 3D coordinate system [43]–[45]. In particular, H and $\{\mathbf{h}_m\}$ induce elevation-dependent path loss and phase variations, which are fully captured in the channel model.

The distance between the source and the center of the coverage area is denoted by $d_{\mathcal{G}} \triangleq \|\rho_{\mathcal{G}}\|_2$, and is assumed to be sufficiently large and the direct transmission path from the source to the UAV-BS is blocked. The aerial-RIS is modeled as a ULA comprising N reflecting elements with inter-element spacing d_{RIS} , and carrier wavelength λ . We assumed an uncoupled model for the RIS elements under this ULA-spacing configuration [46]–[48]. Without loss of generality, the RIS is assumed to be aligned parallel to the x-axis.

Due to the elevated altitude of the aerial-RIS, the backhaul link is assumed to be dominated by an LoS component. Considering that d_{RIS} is significantly smaller than both H and $d_{\mathcal{G}}$, the backhaul link is approximated using a uniform plane-wave model, implying that the path loss is assumed to be identical across all RIS-element pairs. Accordingly, the path loss associated with the source-to-RIS link, $\beta_s(\mathbf{q})$, and the RIS-to-UAV-BS link, $\beta(\mathbf{q}, \rho_m)$, are formulated as [49]:

$$\beta_s(\mathbf{q}) = \beta_0 \|\rho_{\text{RIS}}\|_2^{-2}, \quad \beta(\mathbf{q}, \rho_m) = \beta_0 \|\rho_{\text{RIS}} - \rho_m\|_2^{-2}, \quad (2)$$

where β_0 represents the reference path loss at a 1 m distance. Therefore, the channel for the source-to-RIS link, $\mathbf{H}(\mathbf{q}) \in \mathbb{C}^{N \times M}$, and the RIS-to-destination link, $\mathbf{h}^*(\mathbf{q}, \cdot) \in \mathbb{C}^{1 \times N}$,

are expressed as:

$$\begin{cases} \mathbf{H}(\mathbf{q}) \\ = \sqrt{\beta_s(\mathbf{q})} e^{j\left(\Phi_{\mathbf{H}} - \frac{2\pi\|\rho_{\text{RIS}}\|_2}{\lambda}\right)} \mathbf{a}_{\text{RIS}}(\phi_{\text{r,RIS}}(\mathbf{q})) \mathbf{a}_s^*(\phi_{\text{t,s}}(\mathbf{q})) \\ \mathbf{h}^*(\mathbf{q}, \rho_m) \\ = \sqrt{\beta(\mathbf{q}, \rho_m)} e^{j\left(\Phi_{\mathbf{h}} - \frac{2\pi\|\rho_{\text{RIS}} - \rho_m\|_2}{\lambda}\right)} \mathbf{a}_{\text{RIS}}^*(\phi_{\text{t,RIS}}(\mathbf{q}, \rho_m)), \end{cases} \quad (3)$$

where $\Phi_{\mathbf{H}}$ and $\Phi_{\mathbf{h}}$ are independent and uniformly-distributed random phases within $[0, 2\pi]$. Therein, the array response $\mathbf{a}_s(\cdot)$ and $\mathbf{a}_{\text{RIS}}(\cdot) \in \mathbb{C}^N$ of the source and aerial-RIS, respectively, are given by:

$$\begin{cases} \mathbf{a}_s(\cdot) = \left[\{e^{-j2\pi(m-1)\bar{d}_s(\sin(\cdot))}\}_{m=0}^{M-1} \right]^T \\ \mathbf{a}_{\text{RIS}}(\cdot) = \left[\{e^{-j2\pi(n-1)\bar{d}(\sin(\cdot))}\}_{n=0}^{N-1} \right]^T, \end{cases} \quad (4)$$

where $\bar{d}_s \triangleq \frac{d_s}{\lambda}$ and $\bar{d} \triangleq \frac{d_{\text{RIS}}}{\lambda}$. Lastly, $\phi_{\text{t,s}}(\mathbf{q})$, $\phi_{\text{t,RIS}}(\mathbf{q}, \cdot)$, and $\phi_{\text{r,RIS}}(\mathbf{q})$ denote the angle-of-departure (AoD) of the source-RIS and RIS-destination links and the angle-of-arrival (AoA) of the source-RIS link, respectively. For analytical tractability, it is assumed that the ground source has knowledge of channels, which can be obtained using methods outlined in [50]–[53].

B. Implementation of Active-RIS

Since conventional RIS consists of passive elements which cannot amplify the signal, the reflected signal has to suffer from “multiplicative fading” induced by the multiplication of the path loss of source-to-RIS and RIS-to-UAV-BS links [27], which is presented by $\|\rho_{\text{RIS}}^* - \rho_m\|_2^2 \|\rho_{\text{RIS}}^*\|_2^2$ in (14). Recently, by accompanying the active-RIS [28], [31], [32], [54], we can solve the aforementioned “multiplicative fading” problem by compensating signal power at the active-RIS component.

We assume that, as illustrated in Fig. 1(b), the active amplification circuit with amplification factor $\{\alpha_n\}_{n=1}^N$ and the element-wise hardware power consumption P_E is implemented into the N -element aerial-RIS. In other words, after supplying the hardware power consumption for N active elements, we can generate feasible amplification gain by remaining power

for a given power budget [27], [32]. The reflected and amplified signal \mathbf{y}_{ra} for incident signal \mathbf{x}_{ra} is modeled by [27]:

$$\mathbf{y}_{\text{ra}} = \underbrace{\mathbf{A}\Theta\mathbf{x}_{\text{ra}}}_{\text{Desired signal}} + \underbrace{\mathbf{A}\Theta\mathbf{n}_{\text{a}}}_{\text{Dynamic noise}} + \underbrace{\mathbf{n}_{\text{s}}}_{\text{Static noise}}. \quad (5)$$

Here, $\mathbf{A} \triangleq \text{diag}(\{\alpha_n\}_{n=1}^N)$ is the amplification matrix of the active-RIS, wherein we assume $1 < \alpha_n \leq \alpha_{\max}$ ($\forall n$) [55]. Moreover, $\Theta \triangleq \text{diag}(\{e^{j\theta_n}\}_{n=1}^N) \in \mathbb{C}^{N \times N}$ is a phase shift matrix with phase shift $\theta_n \in [0, 2\pi)$ of the n th element, $\mathbf{n}_{\text{a}} \sim \mathcal{CN}(\mathbf{0}_N, \sigma_{\text{a}}^2 \mathbf{I}_N)$ is the dynamic noise induced by the amplification of the active-RIS elements, and \mathbf{n}_{s} is the static additive Gaussian noise uncorrelated to \mathbf{A} and \mathbf{n}_{a} [27], [31].

By definition, \mathbf{x}_{ra} is given by $\mathbf{x}_{\text{ra}} = \mathbf{H}(\mathbf{q})\mathbf{x}$, where \mathbf{x} is the total transmit signal. We can represent \mathbf{x} as a sum of unit-magnitude precoding vectors $\mathbf{v}_m \in \mathbb{C}^M$, each corresponding to a unit-power signal s_m intended for UAV-BS m , with transmit power P_m at the source. Therefore, \mathbf{x} is:

$$\mathbf{x} = \sum_{m \in \mathbb{M}} \mathbf{v}_m \sqrt{P_m G_s} s_m, \quad (6)$$

which implies that the source transmit power $P_{\text{tot},s}$ is:

$$P_{\text{tot},s} = \mathcal{E} [\|\mathbf{x}\|^2] = \text{tr} (G_s \mathbf{P} \mathbf{V}^* \mathbf{V}) = G_s \sum_{m \in \mathbb{M}} P_m. \quad (7)$$

By (5), the reflection power of active-RIS is given by [26]

$$P_{\text{R}} = \mathcal{E} [\|\mathbf{A}\Theta(\mathbf{x}_{\text{ra}} + \mathbf{n}_{\text{a}})\|_2^2] = \mathcal{E} [\|\mathbf{A}\mathbf{H}(\mathbf{q})\mathbf{x}\|_2^2] + \sigma_{\text{a}}^2 \sum_{n=1}^N \alpha_n^2, \quad (8)$$

and the power consumed by the active hardware components is expressed as $N P_{\text{E}} \triangleq N(P_{\text{DC}} + P_{\text{SW}})$ [28], where P_{E} denotes the per-element hardware power consumption comprising the control and phase-shift switching power P_{SW} and the direct current (DC) biasing power P_{DC} required for the amplifier in each active-RIS element [17]. Consequently, the total power consumption of the active-RIS is given by

$$P_{\text{tot,a}} = P_{\text{R}} + N P_{\text{E}}, \quad (9)$$

where we assume that the efficiency of the power amplifier is 1 in both source and aerial-active-RIS.

Moreover, \mathbf{y}_{ra} faces the channel $\mathbf{h}^*(\mathbf{q}, \boldsymbol{\rho}_m)$ from RIS-destination. Hence, by concatenating the effects, the signal model from source-to-RIS-to-UAV-BS- m is given by [26]

$$y_m = \mathbf{h}^*(\mathbf{q}, \boldsymbol{\rho}_m) \mathbf{A}\Theta\mathbf{H}(\mathbf{q})\mathbf{x} + \mathbf{h}^*(\mathbf{q}, \boldsymbol{\rho}_m) \mathbf{A}\Theta\mathbf{n}_{\text{a}} + n, \quad (10)$$

where $n \sim \mathcal{CN}(0, \sigma^2)$ is the noise at the receiver. By (10), the backhaul rate of UAV-BS m is given by [26]

$$R_m = \frac{B_{\text{b}}}{M_0} \log_2 \left(1 + \underbrace{\frac{P_m G_s |\mathbf{h}^*(\mathbf{q}, \boldsymbol{\rho}_m) \mathbf{A}\Theta\mathbf{H}(\mathbf{q})\mathbf{v}_m|^2}{\sigma_{\text{a}}^2 \|\mathbf{A}\Theta^*\mathbf{h}(\mathbf{q}, \boldsymbol{\rho}_m)\|^2 + \sigma^2}}_{\triangleq \gamma_m} \right), \quad (11)$$

where B_{b} denotes the backhaul bandwidth, which is equally partitioned into M_0 sub-bands assigned to each UAV-BS, and γ_m is the received SNR of UAV-BS m . Here, we can notice the

definition of γ_m that the signal is amplified by $\{\alpha_n\}$ and the denominator is extended with the power of the dynamic noise signal $\mathbf{h}^*(\mathbf{q}, \boldsymbol{\rho}_m) \mathbf{A}\Theta\mathbf{n}_{\text{a}}$. Moreover, since $\mathbf{h}^*(\mathbf{q}, \boldsymbol{\rho}_m)$ contains $\beta(\mathbf{q}, \boldsymbol{\rho}_m) \triangleq \frac{\beta_0}{\|\boldsymbol{\rho}_{\text{RIS}} - \boldsymbol{\rho}_m\|_2^2}$, the effect of the dynamic noise gets weaker when the RIS-to-UAV-BS distance gets larger.

To enhance energy-efficiency by minimizing the source transmit power, i.e., $\sum_{m \in \mathbb{M}} P_m$ [8], [43], which will be clarified in (27), we first derive the precoding vector \mathbf{v}_m for UAV-BS m that maximizes γ_m under a given P_m . This approach enables a reduction in transmit power while maintaining the required data rate, and is formulated by MRT:

$$\mathbf{v}_m = \frac{\mathbf{a}_s(\phi_{\text{t,s}}(\mathbf{q}))}{\sqrt{M}} \quad (\forall m \in \mathbb{M}), \quad (12)$$

which implies that the optimal transmission strategy $\{\mathbf{v}_m\}_{m \in \mathbb{M}}$ is given to maximize the inner-product with $\mathbf{a}_s^*(\phi_{\text{t,s}}(\mathbf{q}))$ [43]. Moreover, in (11) it is clear that

$$\|\mathbf{A}\Theta^*\mathbf{h}(\mathbf{q}, \boldsymbol{\rho}_m)\|_2^2 = \|\mathbf{A}\mathbf{h}(\mathbf{q}, \boldsymbol{\rho}_m)\|_2^2 = \beta(\mathbf{q}, \boldsymbol{\rho}_m) \sum_{n=1}^N \alpha_n^2, \quad (13)$$

where the first equality comes from the fact that $\Theta \triangleq \text{diag}(\{e^{j\theta_n}\}_{n=1}^N)$ is unitary. By applying MRT and (13), γ_m becomes (14) where $\bar{\gamma} \triangleq \frac{P_m G_s \beta_0^2 M}{\sigma_{\text{a}}^2 \beta(\mathbf{q}, \boldsymbol{\rho}_m) \sum_{n=1}^N \alpha_n^2 + \sigma^2}$ [43].

For $\{\theta_n^*\}_{n=1}^N$ to maximize γ_m for a given P_m , they must be configured to ensure that the reflected signals are constructively combined at the designated point $\boldsymbol{\rho}_m$:

$$\begin{aligned} \theta_n^*(\mathbf{q}, \boldsymbol{\rho}_m) &= \bar{\theta} - 2\pi(n-1)\bar{d}(\sin(\phi_{\text{t,RIS}}(\mathbf{q}, \boldsymbol{\rho}_m)) - \sin(\phi_{\text{r,RIS}}(\mathbf{q}))), \end{aligned} \quad (15)$$

where $\bar{\theta}$ is a random phase shift in RIS. However, since M_0 UAV-BSs need to be served, the optimal $\{\theta_n^*\}_{n=1}^N$ vary for each $m \in \mathbb{M}$. Therefore, it is necessary to determine a phase alignment point $\bar{\boldsymbol{\rho}}$ that achieves a Pareto-optimal solution with respect to $\{\gamma_m\}_{m \in \mathbb{M}}$. That is, for given \mathbf{q} and $\bar{\boldsymbol{\rho}}$, the phase shifts $\{\theta_n^*\}_{n=1}^N$ are set as

$$\begin{aligned} \theta_n^*(\mathbf{q}, \bar{\boldsymbol{\rho}}) &= \bar{\theta} - 2\pi(n-1)\bar{d}(\sin(\phi_{\text{t,RIS}}(\mathbf{q}, \bar{\boldsymbol{\rho}})) - \sin(\phi_{\text{r,RIS}}(\mathbf{q}))), \end{aligned} \quad (16)$$

which coherently overlaps the reflected signal to $\bar{\boldsymbol{\rho}}$. By substituting (16) into (14), γ_m becomes

$$\gamma_m = \bar{\gamma} \frac{\tilde{g}(\Delta\phi_m(\bar{\boldsymbol{\rho}}))}{\|\boldsymbol{\rho}_{\text{RIS}} - \boldsymbol{\rho}_m\|_2^2 \|\boldsymbol{\rho}_{\text{RIS}}\|_2^2}, \quad (17)$$

where $\tilde{g}(\Delta\phi_m(\bar{\boldsymbol{\rho}}))$ represents the passive beamforming gain of the aerial-active-RIS towards $\boldsymbol{\rho}_m$, assuming that the phases are aligned with $\bar{\boldsymbol{\rho}}$. This gain is derived by evaluating

$$\tilde{g}(\Delta\phi_m(\bar{\boldsymbol{\rho}})) = \left| \sum_{n=1}^N \alpha_n e^{j(2\pi(n-1)\bar{d}\Delta\phi_m(\bar{\boldsymbol{\rho}}))} \right|^2 \quad (18)$$

in (14), where $\Delta\phi_m(\bar{\boldsymbol{\rho}})$ is the sin-AoD deviation between $\bar{\boldsymbol{\rho}}$ and $\boldsymbol{\rho}_m$, that is, $\Delta\phi_m(\bar{\boldsymbol{\rho}}) \triangleq \sin(\phi_{\text{t,RIS}}(\mathbf{q}, \boldsymbol{\rho}_m)) - \sin(\phi_{\text{t,RIS}}(\mathbf{q}, \bar{\boldsymbol{\rho}}))$. As depicted in Fig. 2(a), the optimal beamforming gain is achieved within the main lobe of \tilde{g} . Moreover,

$$\gamma_m = \bar{\gamma} \left| \mathbf{h}^*(\mathbf{q}, \boldsymbol{\rho}_m) \mathbf{A} \boldsymbol{\Theta} \mathbf{H}(\mathbf{q}) \frac{\mathbf{a}_s(\phi_{t,s}(\mathbf{q}))}{\sqrt{M}} \right|^2 = \bar{\gamma} \frac{\left| \sum_{n=1}^N \alpha_n e^{j(\theta_n + 2\pi(n-1)\bar{d}(\sin(\phi_{t,RIS}(\mathbf{q}, \boldsymbol{\rho}_m)) - \sin(\phi_{r,RIS}(\mathbf{q}))))} \right|^2}{\|\boldsymbol{\rho}_{RIS}\|_2^2 \|\boldsymbol{\rho}_{RIS} - \boldsymbol{\rho}_m\|_2^2}, \quad (14)$$

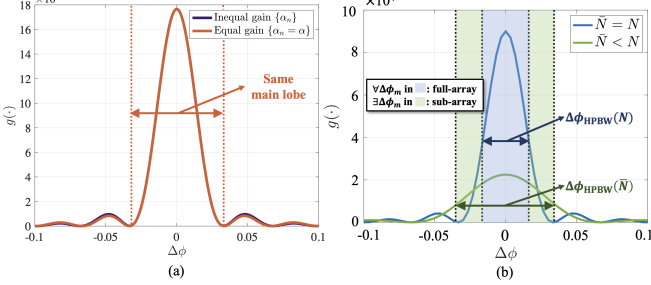


Fig. 2. Illustration of passive beamforming gain g and the full/sub-array structure: (a) The main lobe characteristics obtained under a general unequal gain configuration $\{\alpha_n\}_{n=1}^N$ are nearly identical to those under the equal-gain case $\alpha_n = \alpha$ ($\forall n$). (b) When the sin-AoD deviation lies beyond the HPBW of the full-array beamforming pattern, a sub-array structure is employed to accommodate the deviated point.

Fig. 2(a) demonstrates that adopting the equal active-RIS gain scenario yields nearly identical results within the main lobe region. This observation is actually rigorously true, which can be proved by the triangular and Cauchy-Schwartz inequality,

$$\tilde{g}(\Delta\phi) \leq \left(\sum_{n=1}^N \alpha_n \right)^2 \leq N \sum_{n=1}^N \alpha_n^2, \quad (19)$$

respectively, with the first inequality becoming tight when $\Delta\phi$ is sufficiently small (main-lobe region) so that the phasors are nearly aligned. In our deployment, the aerial-active-RIS is placed close to the source and the beam is steered towards $\bar{\rho}$ chosen to represent the Pareto-optimal directions of the UAV-BSs; consequently, $\Delta\phi_m(\bar{\rho})$ stays within the main-lobe vicinity and the variation of the denominator term is minor. In this regime, maximizing \tilde{g} is equivalently achieved by uniform $\alpha_n = \alpha$ by the second inequality, which yields the dominant gain improvement while avoiding an ill-conditioned optimization over element-wise amplitudes that provides marginal additional benefit, as it matches with Fig 2(a).

Considering $\alpha_n = \alpha$ ($\forall n$) and $\bar{N} (\leq N)$ utilized active-RIS elements, \tilde{g} becomes

$$\tilde{g} = \alpha^2 g(\Delta\phi_m(\bar{\rho})) \triangleq \alpha^2 \left| \frac{\sin(\pi \bar{N} \bar{d} \Delta\phi_m(\bar{\rho}))}{\sin(\pi \bar{d} \Delta\phi_m(\bar{\rho}))} \right|^2, \quad (20)$$

As in Fig. 2(b), g dissipates to 0 out of its HPBW $\Delta\phi_{HPBW}(\bar{N})$ [56]:

$$\Delta\phi_{HPBW}(\bar{N}) \approx \frac{0.8858}{\bar{N} \bar{d}}, \quad \Delta\phi_{HPBW}(N) \triangleq \Delta\phi_{HPBW}, \quad (21)$$

and the peak gain of g is \bar{N}^2 . Thus, it is necessary to fine-tune $\bar{\rho}$ and determine the maximum value of \bar{N} to locate every UAV-BS within the HPBW, thereby maximizing $\{g(\Delta\phi_m(\bar{\rho}))\}_{m \in \mathbb{M}}$.

Moreover, $\bar{\gamma}$ is transformed into

$$\bar{\gamma} \triangleq \frac{P_m G_s \beta_0^2 M}{\sigma_a^2 \beta(\mathbf{q}, \boldsymbol{\rho}_m) N \alpha^2 + \sigma^2}. \quad (22)$$

and we can also manipulate (8) by (23). By adding NP_E to (23) [32], it implies that for given α^2 , G_s , N , and P_E , the maximum power constraint of active-RIS is given by

$$P_{\text{tot,a}} = P_R + NP_E = \alpha^2 \left(NM \beta_s G_s \sum_{m \in \mathbb{M}} P_m + N \sigma_a^2 \right) + NP_E \leq P_{\text{max,a}}, \quad (24)$$

where $P_{\text{max,a}}$ is the maximum threshold of the active-RIS reflection power. From (24), the trade-off between α^2 and the consumed power becomes explicit. Increasing α^2 directly raises the required P_R , which in turn tightens $P_{\text{max,a}}$. Consequently, the feasible power budget for signal transmission ($\sum_{m \in \mathbb{M}} P_m$) is reduced, thereby limiting the admissible $\{P_m\}$ and reflecting the inherent trade-off between higher amplification gain and increased aerial-active-RIS power consumption.

To reliably support the UAV-BSs, the backhaul rate $\{R_m\}_{m \in \mathbb{M}}$ provided by the source should be balanced with the throughput $\{C_m\}_{m \in \mathbb{M}}$ of the fronthaul link: $R_m = C_m$ ($\forall m \in \mathbb{M}$), where the balance between fronthaul and backhaul capacities is critical for optimal network performance with avoidance of bottleneck in B5G/6G wireless network [43], [57]. By $R_m = \frac{B_b}{M_0} \log_2(1 + \gamma_m)$, P_m must satisfy the following constraint (25). Moreover, the maximum power budget of the source and aerial-active-RIS is given by [32], [58]

$$(1) : P_{\text{tot,s}} = G_s \sum_{m \in \mathbb{M}} P_m \leq P_{\text{max}}, \quad (2) : (24), \quad (26)$$

respectively, wherein $\mathbf{V} \triangleq [\mathbf{v}_1 \cdots \mathbf{v}_{M_0}] \in \mathbb{C}^{M \times M_0}$ derived by (12), $\mathbf{P} \triangleq \text{diag}(\{P_m\}_{m \in \mathbb{M}}) \in \mathbb{R}^{M_0 \times M_0}$ and P_{max} is the feasible threshold of the source transmit power, respectively.

The definition of energy-efficiency is given by [58]

$$\eta \triangleq \frac{\sum_{m \in \mathbb{M}} C_m}{\underbrace{\sum_{m \in \mathbb{M}} (P_m + P_{\text{UAV-BS},m}) + P_{\text{tot,a}} + P_{\text{gBS}} + P_{\text{AP}}}_{\triangleq P_0}}, \quad (27)$$

where the $\sum_{m \in \mathbb{M}} C_m$ comes from $R_m = C_m$ ($\forall m \in \mathbb{M}$), and P_{AP} , P_{gBS} and $\sum_{m \in \mathbb{M}} P_{\text{UAV-BS},m}$ are the hardware-dissipated power used by the aerial platform that carries active-RIS, ground backhaul source and the UAV-BS m , respectively. Hence, since the numerator $\sum_{m \in \mathbb{M}} R_m$ becomes constant since the backhaul rate $\{R_m\}_{m \in \mathbb{M}}$ is balanced with the fronthaul throughput $\{C_m\}_{m \in \mathbb{M}}$, we can conclude that the energy-efficiency maximization problem is equivalent to

$$P_R = \alpha^2 \left(N\beta_s \mathcal{E} \left[\left| \mathbf{a}_s^*(\phi_{t,s}(\mathbf{q})) \sum_{m \in \mathbb{M}} \frac{\mathbf{a}_s(\phi_{t,s}(\mathbf{q}))}{\|\mathbf{a}_s(\phi_{t,s}(\mathbf{q}))\|_2} \sqrt{P_m G_s} s_m \right|^2 \right] + N\sigma_a^2 \right) = \alpha^2 \left(NM\beta_s G_s \sum_{m \in \mathbb{M}} P_m + N\sigma_a^2 \right) \quad (23)$$

$$P_m = \alpha^{-2} \left(2^{\frac{M_0}{B_b} C_m} - 1 \right) \frac{\left(\sigma^2 + \alpha^2 \sigma_a^2 N \frac{\beta_0}{\|\boldsymbol{\rho}_{\text{RIS}} - \boldsymbol{\rho}_m\|_2^2} \right) \|\boldsymbol{\rho}_{\text{RIS}} - \boldsymbol{\rho}_m\|_2^2 \|\boldsymbol{\rho}_{\text{RIS}}\|_2^2}{G_s \beta_0^2 M g(\Delta\phi_m(\bar{\boldsymbol{\rho}}))} \quad (\forall m \in \mathbb{M}) \quad (25)$$

the minimization of P_0 , the total power consumption of the whole system. From the denominator of (27), P_0 includes P_{AP} , P_{GBS} and $\sum_{m \in \mathbb{M}} P_{\text{UAV-BS},m}$. In this paper, we adopt two key assumptions: (i) the transmit amplifiers operate within their linear region, and (ii) the circuit power consumption is independent of the communication rate [58]–[60]. These assumptions are valid for most practical wireless communication systems [28], [32], [58], where amplifiers are typically designed to work within the linear portion of their transfer function, and where the hardware power consumption P_{AP}^2 , P_{BS} and $\{P_{\text{UAV-BS},m}\}_{m \in \mathbb{M}}$ can be treated as constant offsets. Therefore, together with $\sum_{m \in \mathbb{M}} R_m = \sum_{m \in \mathbb{M}} C_m$, we exclude them from the energy-efficiency maximization process, and consider

$$\text{obj} \triangleq \sum_{m \in \mathbb{M}} P_m + P_{\text{tot,a}}, \quad (28)$$

which is total transmit and operation (reflection + hardware components) power of the source and aerial-active-RIS, respectively, as a objective function of the energy-efficiency maximization, which can be formulated by (29). From now on, we will use term “total power” as (28).

Remark 1. Since $C_m > 0$, $\|\boldsymbol{\rho}_{\text{RIS}}\|_2 \geq H > 0$ and $\|\boldsymbol{\rho}_{\text{RIS}} - \boldsymbol{\rho}_m\|_2 > 0$ ($\because \boldsymbol{\rho}_{\text{RIS}}$ is extremely close to the origin, as shown in *Theorem 1* and Fig. 5). Thereby, the right-hand side (RHS) of (25) is non-zero, thus ensuring non-zero transmit power for every UAV-BS via aerial-active-RIS.

III. PROPOSED ALGORITHM

A. Minimizing the Numerator

Problem (29) is highly nonlinear and non-convex due to its highly-cluttered RHS_1 and RHS_2 of the constraints. Therefore, we will approach the problem by first assuming that α is given, and minimizing the numerator and maximizing the denominator of RHS_1 , respectively, which leads to the minimization of the objective function. After that, we will minimize the total power with respect to α . Through numerical simulations, we will show that the second constraint, which represents the upper-bound of the source transmit power, does not impact the feasibility of the problem. Therefore, our approach of focusing primarily on the first constraint is justified for energy-efficiency minimization.

It first leads to minimizing the numerator of RHS_1 . For given α , if we multiply $1 + \alpha^2 NM\beta_s G_s$ to the both sides

²Since we assumed that aerial platform is fixed (hovering), the consumed power, which is in general a function of velocity, becomes constant [61].

of the first constraint of (29), which becomes the first term of the objective function in (29) related to $\sum_{m \in \mathbb{M}} P_m$, it becomes (30). Hence, the RHS of (30) is determined by

$$(\|\boldsymbol{\rho}_{\text{RIS}}\|_2^2 + \tilde{\Omega}_1)(\|\boldsymbol{\rho}_{\text{RIS}} - \boldsymbol{\rho}_m\|_2^2 + \tilde{\Omega}_2), \quad (31)$$

where

$$\tilde{\Omega}_1 = \alpha^2 NM\beta_0 G_s, \quad \tilde{\Omega}_2 = \alpha^2 \frac{\sigma_a^2}{\sigma^2} N\beta_0. \quad (32)$$

Thereafter, by letting \mathbf{q}_m the 2D location of the aerial-active-RIS considering only UAV-BS m ($\boldsymbol{\rho}_{\text{RIS}} = [\mathbf{q}_m^T \ H]^T$), the numerator minimization becomes equivalent to:

$$\begin{aligned} \min_{\mathbf{q}_m} & (\|\boldsymbol{\rho}_{\text{RIS}}\|_2^2 + \tilde{\Omega}_1)(\|\boldsymbol{\rho}_{\text{RIS}} - \boldsymbol{\rho}_m\|_2^2 + \tilde{\Omega}_2) \\ & = \left(H^2 + \|\mathbf{q}_m\|_2^2 + \tilde{\Omega}_1 \right) \left((H - h_m)^2 + \|\mathbf{q}_m - \mathbf{w}_m\|_2^2 + \tilde{\Omega}_2 \right) \\ & \text{s.t. } \|\mathbf{q}_m\|_2 \ll \delta \|\mathbf{w}_m\|_2, \end{aligned} \quad (33)$$

where $\delta \ll 1$ is constant. The constraint “ $\|\mathbf{q}_m\|_2 \ll \delta \|\mathbf{w}_m\|_2$ ” is imposed to keep \mathbf{q}_m near the source. Positioning \mathbf{q}_m with fixed H close to the source ensures that the full-array RIS architecture ($\bar{N} = N$) is almost certainly utilized, which maximizes the minimum SNR [46] and consequently reduces the total transmit power $(1 + \alpha^2 NM\beta_s G_s) \sum_{m \in \mathbb{M}} P_m$. Fortunately, we can find a practical solution for the problem, as stated in *Theorem 1*.

Theorem 1. *The solution of Problem (33) is given by*

$$\mathbf{q}_m^* = \kappa_m \mathbf{w}_m, \quad (34)$$

where

$$\kappa_m = \frac{1}{2} + 2\sqrt{-\frac{a}{3}} \cos \left(\frac{1}{3} \cos^{-1} \left(\frac{3b}{2a} \sqrt{-\frac{3}{a}} \right) - \frac{4}{3}\pi \right). \quad (35)$$

Here, a and b are given by

$$a \triangleq \frac{1}{2} (\zeta_1^2 + \zeta_2^2 + \bar{\Omega}_1 + \bar{\Omega}_2) - \frac{1}{4}, \quad b \triangleq \frac{1}{4} (\zeta_2^2 - \zeta_1^2 + \bar{\Omega}_2 - \bar{\Omega}_1), \quad (36)$$

where

$$\zeta_1 \triangleq \frac{H}{\|\mathbf{w}_m\|_2}, \quad \zeta_2 \triangleq \frac{|H - h_m|}{\|\mathbf{w}_m\|_2}, \quad \bar{\Omega}_i \triangleq \|\mathbf{w}_m\|_2^{-2} \tilde{\Omega}_i \quad (i = 1, 2). \quad (37)$$

Proof. See Appendix A. ■

We numerically confirm in Section IV that κ_m remains positive yet very close to zero under the given assumptions,

$$\begin{aligned}
& \min_{q, \bar{\rho}, \{\bar{N}\}, \alpha, \{P_m\}_{m \in \mathbb{M}}} (1 + \alpha^2 NM \beta_s G_s) \sum_{m \in \mathbb{M}} P_m + \alpha^2 N \sigma_a^2 + N P_E \quad (\triangleq \text{obj}) \\
& \text{s.t. } P_m = \alpha^{-2} \left(2^{\frac{M_0}{B_b} C_m} - 1 \right) \frac{\left(\sigma^2 + \alpha^2 \sigma_a^2 N \frac{\beta_0}{\|\rho_{\text{RIS}} - \rho_m\|_2^2} \right) \|\rho_{\text{RIS}} - \rho_m\|_2^2 \|\rho_{\text{RIS}}\|_2^2}{G_s \beta_0^2 M g(\Delta \phi_m(\bar{\rho}))} \quad (\triangleq \text{RHS}_1) \quad (\forall m \in \mathbb{M}), \\
& \sum_{m \in \mathbb{M}} P_m \leq \min \{ G_s^{-1} P_{\max}, \alpha^{-2} G_s^{-1} N^{-1} M^{-1} \beta_s^{-1} (P_{\max, a} - N P_E - \alpha^2 N \sigma_a^2) \} \quad (\triangleq \text{RHS}_2)
\end{aligned} \tag{29}$$

$$\begin{aligned}
& (1 + \alpha^2 NM \beta_s G_s) P_m \\
& = \alpha^{-2} \left(2^{\frac{M_0}{B_b} C_m} - 1 \right) \frac{\left(1 + \alpha^2 NM \frac{\beta_0}{\|\rho_{\text{RIS}}\|_2^2} G_s \right) \left(\sigma^2 + \alpha^2 \sigma_a^2 N \frac{\beta_0}{\|\rho_{\text{RIS}} - \rho_m\|_2^2} \right) \|\rho_{\text{RIS}} - \rho_m\|_2^2 \|\rho_{\text{RIS}}\|_2^2}{G_s \beta_0^2 M g(\Delta \phi_m(\bar{\rho}))} \quad (\forall m \in \mathbb{M})
\end{aligned} \tag{30}$$

thereby validating that $\mathbf{q}_m^* = \kappa_m \mathbf{w}_m$ serves as an appropriate solution for the proposed power-minimization procedure.

After obtaining $\{\mathbf{q}_m^*\}_{m \in \mathbb{M}}$, we need to determine a single \mathbf{q}^* that achieves a Pareto-optimal for all $m \in \mathbb{M}$ in relation to (33). We adopt a global criterion approach that minimizes the total ℓ_2 -distances, thereby guiding the solution toward the Pareto front [62].

$$\min_q \sum_{m \in \mathbb{M}} \|\mathbf{q}_m^* - \mathbf{q}\|_2. \tag{38}$$

Problem (38) is known as the Fermat-Torricelli problem, which is convex and can therefore be efficiently solved using Weiszfeld's algorithm [63] with guaranteeing the optimal solution [64]. Consequently, by solving (38), we obtain \mathbf{q}^* , which serves as a suboptimal solution for the numerator minimization. The obtained \mathbf{q}^* provides a clear deployment insight: the aerial-active-RIS should be placed sufficiently closer to the source in terms of 2D distance to enhance the incident signal power, while maintaining a moderate distance from the UAV-BSs to balance the overall power consumption.

Remark 2. To keep $\|\mathbf{q}^*\|_2$ small even in the presence of an outlier within $\{\mathbf{q}_m^*\}_{m \in \mathbb{M}}$, we minimize the sum of norms rather than the squared norms in (38), which further enhances the robustness of the solution [62].

B. Maximizing the Denominator

We adopt the same methodology as described in Section III.B of [46] to solve the denominator (29) since the denominator is exactly same with the passive-RIS-implemented scenario in [46]. This allows us to determine the sub-optimal values for $\{\bar{N}\}$, $\bar{\rho}$ (or $\{\bar{\rho}_i^*\}_{i=1}^L$), and Θ for utilizing both full RIS array or L -times partitioned sub-array scenario.

C. Determining α and $\{P_m\}_{m \in \mathbb{M}}$

Since we have determined \mathbf{q}^* , $\{\bar{N}\}$, $\bar{\rho}$ (or $\{\bar{\rho}_i^*\}_{i=1}^L$), Θ , the optimal α^* is determined by following *Theorem 2*.

Theorem 2. For given \mathbf{q}^* , $\{\bar{N}\}$, $\bar{\rho}$ (or $\{\bar{\rho}_i^*\}_{i=1}^L$), Θ , the optimum α that minimizes obj is given by

$$\alpha^* = \min \left\{ \sqrt[4]{\frac{\sum_{m \in \mathbb{M}} \Omega_0 \|\rho_{\text{RIS}}\|_2^2 \|\rho_{\text{RIS}} - \rho_m\|_2^2}{N \sigma_a^2 + \sum_{m \in \mathbb{M}} \Omega_0 \Omega_1 \Omega_2}}, \alpha_{\max} \right\}, \tag{39}$$

where

$$\Omega_0 = \sigma^2 \frac{2^{\frac{M_0}{B_b} C_m} - 1}{G_s \beta_0^2 M g(\Delta \phi_m^*)} \tag{40}$$

$$\Omega_1 = \alpha^{-2} \tilde{\Omega}_1 = NM \beta_0 G_s, \quad \Omega_2 = \alpha^{-2} \tilde{\Omega}_2 = \frac{\sigma_a^2}{\sigma^2} N \beta_0.$$

Proof. See Appendix B. ■

Since we determine all the variables $\mathbf{q}, \bar{\rho}, \{\bar{N}\}, \alpha^*$, the power $\{P_m\}_{m \in \mathbb{M}}$ is given by RHS_1 , which can be expressed by (42), where $\rho_{\text{RIS}}^* = [\mathbf{q}^{*\text{T}} \ H]^{\text{T}}$ and $\Delta \phi_m^*$ is defined by

$$\Delta \phi_m^* \triangleq \begin{cases} \Delta \phi_m(\bar{\rho}^*) & (\bar{N} = N \text{ (full-array)}) \\ \Delta \phi_m(\bar{\rho}_i^*) & (\bar{N} < N \text{ (sub-array, } m \in \mathbb{M}_i\text{)}) \end{cases}, \tag{41}$$

where the full- and L -times-partitioned sub-array scenario with phase-align points $\{\bar{\rho}_i^*\}_{i=1}^L$ and partitions of UAV-BS $\{\mathbb{M}_i\}_{i=1}^L$ ($\cup_i \mathbb{M}_i = \mathbb{M}$) are defined in Section III.B in [43]. Thus, by substituting (42) and α^* to obj , we can achieve the optimal total power by utilizing aerial-active-RIS.

D. Conditions for Feasibility

Although the power is to be positive in *Remark 1*, we cannot claim the strict feasibility since we cannot always guarantee the upper-bound of $\sum_{m \in \mathbb{M}} P_m$ by (42). Specifically, the backhaul-rate-ensuring constraint leads to:

$$R_m = C_m \rightarrow P_m = [\text{RHS}_1]_m \quad (\forall m \in \mathbb{M}), \tag{43}$$

where $[\text{RHS}_1]_m$ is the RHS_1 corresponding to P_m in the first constraint of (29), and the source/active-RIS power constraint is trivially given by

$$\sum_{m \in \mathbb{M}} P_m \leq \text{RHS}_2. \tag{44}$$

$$P_m^* = \alpha^{*-2} \left(2^{\frac{M_0}{B_b} C_m} - 1 \right) \frac{\left(\sigma^2 + \alpha^{*2} \sigma_a^2 N \frac{\beta_0}{\|\boldsymbol{\rho}_{\text{RIS}}^* - \boldsymbol{\rho}_m\|_2^2} \right) \|\boldsymbol{\rho}_{\text{RIS}}^* - \boldsymbol{\rho}_m\|_2^2 \|\boldsymbol{\rho}_{\text{RIS}}^*\|_2^2}{G_s \beta_0^2 M g(\Delta\phi_m^*)} \quad (\forall m \in \mathbb{M}) \quad (42)$$

From (43) and (44), it is clear that although the individual transmit power meets the constraint in (43) by choosing the lower-bound itself as a transmit power value, we cannot guarantee $\sum_{m \in \mathbb{M}} [\text{RHS}_1]_m \leq \text{RHS}_2$ [58], [65], [66]. We, however, offer some additional clarification on whether the feasibility holds or not. Using the closed-form rate-matching transmit power in (42), the total source transmit power can be expressed as

$$\sum_{m \in \mathbb{M}} P_m^* = \frac{d_s^2}{G_s \beta_0^2 M} \left(\alpha^{-2} \sigma^2 \sum_{m \in \mathcal{M}} \frac{\Gamma_m d_m^2}{g_m} + \sigma_a^2 N \beta_0 \sum_{m \in \mathcal{M}} \frac{\Gamma_m}{g_m} \right), \quad (45)$$

where $\Gamma_m \triangleq 2^{\frac{M_0}{B_b} C_m} - 1$, $d_s^2 = \|\boldsymbol{\rho}_{\text{RIS}}^*\|_2^2$, $d_m^2 = \|\boldsymbol{\rho}_{\text{RIS}}^* - \boldsymbol{\rho}_m\|_2^2$, and $g_m = g(\Delta\phi_m^*)$. Substituting (45) into the two terms in the left-hand side in (29) yields two sufficient feasibility conditions with respect to RHS_2 .

(1. Source power budget P_{max})

$$P_{\text{max}} \geq \frac{d_s^2}{\beta_0^2 M} \left(\alpha^{-2} \sigma^2 \sum_{m \in \mathcal{M}} \frac{\Gamma_m d_m^2}{g_m} + \sigma_a^2 N \beta_0 \sum_{m \in \mathcal{M}} \frac{\Gamma_m}{g_m} \right). \quad (46)$$

(2. Aerial-Active-RIS power budget $P_{\text{max},a}$)

$$P_{\text{max},a} \geq N P_E + \alpha^2 N \sigma_a^2 + N \beta_s \frac{d_s^2}{\beta_0^2} \left(\sigma^2 \sum_{m \in \mathcal{M}} \frac{\Gamma_m d_m^2}{g_m} + \alpha^2 \sigma_a^2 N \beta_0 \sum_{m \in \mathcal{M}} \frac{\Gamma_m}{g_m} \right). \quad (47)$$

Equations (46) and (47) provide an explicit post-solution feasibility check:

- Once the optimal variables are obtained, $\sum_m P_m^*$ is evaluated via (45)
- The constraint $\sum_m P_m^* \leq \text{RHS}_2$ is verified by checking (46) and (47).

Equation (45) reveals that $\sum_m P_m^*$ consists of two components: an α^{-2} -decreasing term associated with thermal noise and an α -independent floor term induced by the amplified dynamic noise. Consequently, increasing α does not cause $\sum_m P_m^*$ to diverge. Furthermore, when the phase-alignment/partitioning design keeps all UAV-BSs within the RIS main lobe, the passive beamforming gain satisfies $g_m \simeq N^2$ [43]. In this regime,

$$\sum_m \frac{\Gamma_m}{g_m} \approx \frac{1}{N^2} \sum_m \Gamma_m, \quad \sum_m \frac{\Gamma_m d_m^2}{g_m} \approx \frac{1}{N^2} \sum_m \Gamma_m d_m^2, \quad (48)$$

so that the last term of the right-hand side in both (46) and (47) scale down with N . In Section IV (Fig. 8), we verify that the practical transmit power and total power obtained by the proposed algorithm remain well below the feasible threshold, achieving a feasibility rate of 100% even with conservative power budget. This confirms the almost-sure feasibility of our approach, thereby rendering the consideration of infeasible scenarios negligible.

TABLE I
SIMULATION PARAMETERS

Parameter	Description	Value
B_b	Bandwidth of the backhaul link (unless referred)	50 (MHz)
M_0	Number of UAV-BSs	$\gtrsim 4$ [8]
\mathcal{G}	Targeted urban region	500×500 (m)
$\boldsymbol{\rho}_{\mathcal{G}}$	Center of \mathcal{G} (unless referred)	$[1000 \ 0]^T$ (m)
$(P_{\text{max}}, P_{\text{max},a})$	Feasible threshold of source transmit power and active-RIS power consumption	20 (dBm) [32]
G_{max}	Maximum directional gain	8 (dB)
H	Height of aerial-RIS (unless referred)	180 (m)
N	Number of RIS elements (unless referred)	300
M	Number of source antennas	16
(d_s, d_{RIS})	Source antenna and RIS element separations	$\left(\frac{\lambda}{2}, \frac{\lambda}{10}\right)$ [67]
α_{max}^2	Maximum amplification gain of the active-RIS	40 (dB) [32]
P_E	Power consumed by single active hardware component	-3.8 (dBm) [28], [32]
Δ_0	Distance from α^{*2} in dB for non-optimality comparison	-5 (dB)
σ_a^2	Dynamic noise of the active-RIS elements	-80 (dBm) [28], [32]

E. Analysis on Computational Complexity

The computational complexity of the proposed algorithm is divided into three main stages. In Section III.A, we begin by selecting $\{\kappa_m\}_{m \in \mathbb{M}}$ according to (35), which involves a complexity of $\mathcal{O}(M_0)$. Subsequently, we solve for \mathbf{q}^* using (38), which has an upper-bounded complexity of $\mathcal{O}(I_{\mathbb{M}} M_0)$, where $I_{(\cdot)}$ represents the number of iterations required by Weiszfeld's algorithm for the given set [43], [63], [64]. In Section III.B, the complexity is identical to that presented in Section III.B of [43], and is given by $\mathcal{O}((L_{\text{max}} + I_L + M_0) M_0 + L)$. Here, L_{max} denotes the maximum candidate for L , identified through a one-dimensional search, and $I_L \triangleq \max_{i \in \{1, \dots, L\}} I_{\mathbb{M}_i}$. The RIS phase alignment step, performed via (16), incurs a complexity of $\mathcal{O}(N)$. Lastly, in Section III.C, we optimize α^* and $\{P_m^*\}_{m \in \mathbb{M}}$ through (39) and (42), each requiring $\mathcal{O}(M_0)$. Thus, the overall computational complexity is bounded as

$$\begin{aligned} & \mathcal{O}((I_{\mathbb{M}} + L_{\text{max}} + I_L + M_0) M_0 + L + N) \\ & \approx \mathcal{O}((I_{\mathbb{M}} + I_L + M_0) M_0 + N) \quad (\because I_{(\cdot)} > L_{\text{max}} \geq L), \end{aligned} \quad (49)$$

which is within quadratic order. Therefore, we can conclude that the proposed algorithm is both energy-efficient and computationally efficient.

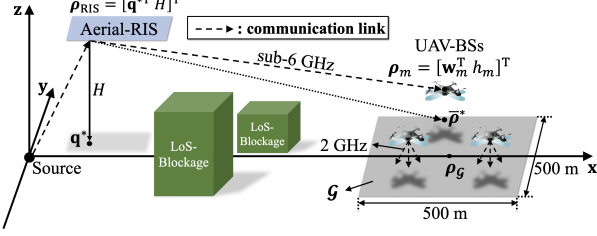


Fig. 3. Simulated aerial-active-RIS configuration with an N -element active-RIS and M_0 UAV-BSs.

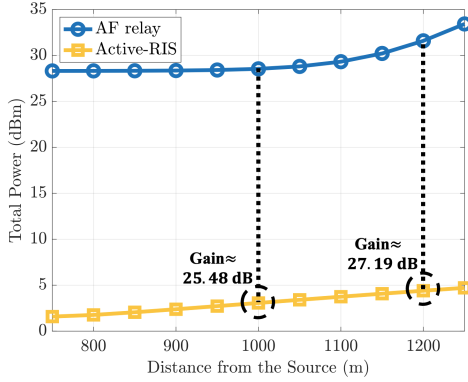


Fig. 4. Simulated aerial-active-RIS configuration compared to M -array aerial-AF-relay.

IV. NUMERICAL RESULTS

A. Simulation Setup

We considered 10^3 independent realizations of randomly distributed users and their associated UAV-BSs [8]. The fronthaul and backhaul links were assumed to operate over 2 GHz and sub-6 GHz frequency bands, respectively [68]. Furthermore, the directional antennas at source were assumed to follow the radiation pattern described in [68]. Accordingly, the directional antenna gain $G_s(\theta, \phi)$ with maximum directional gain G_{\max} can be expressed as

$$G_s(\theta, \phi) = G_{\max} - \min(A_v(\theta) + A_h(\phi), A_{\max}). \quad (50)$$

where the vertical and horizontal attenuations A_v and A_h , respectively, are given by

$$\begin{cases} A_v(\theta) = \min\left(12\left(\frac{\theta-90^\circ}{\theta_H}\right)^2, \text{SLA}_v\right) \\ A_h(\phi) = \min\left(12\left(\frac{\phi}{\phi_H}\right)^2, A_{\max}\right), \end{cases} \quad (51)$$

where $\theta \in [0^\circ, 180^\circ]$ and $\phi \in [-180^\circ, 180^\circ]$ denote the vertical and horizontal angles, θ_H and ϕ_H represent the HPBWs in the vertical and horizontal domains, respectively, and SLA_v and A_{\max} denote the vertical side-lobe and maximum attenuations, respectively.

Under this setup, we conducted a numerical performance comparison between the proposed aerial-active-RIS scheme and the passive-RIS-based algorithm in [43], which aims to minimize the transmit power at the source. Under same achiev-

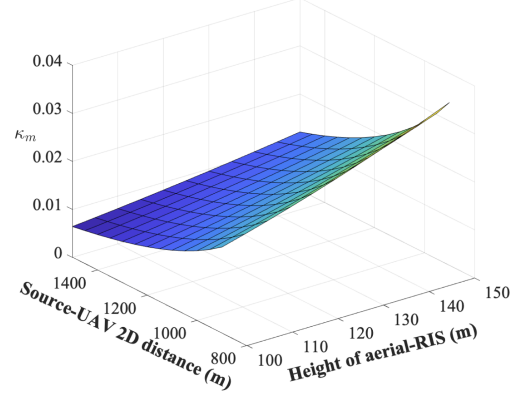


Fig. 5. Variation of κ_m as a function of the aerial-active-RIS altitude and the 2D source-UAV distance with $h_m = 45$ m.

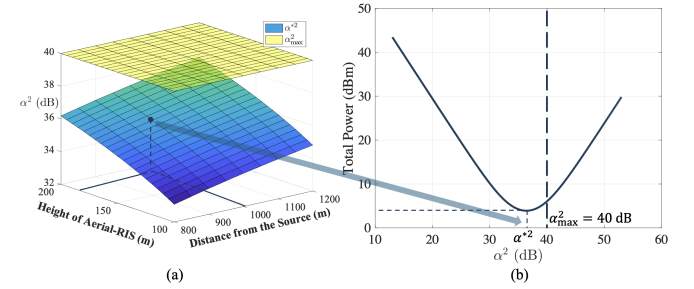


Fig. 6. Behavior of (a) α^*2 with $\alpha^2_{\max} = 40$ dB with respect to the height of aerial-RIS and the source-UAV 2D distance and (b) optimal total power with respect to α^2 with minimum at α^*2 .

able rate $\{C_m\}_{m \in \mathbb{M}}$, the energy-efficiency η_p for passive-RIS is given by [43], [58]

$$\eta_p = \frac{\sum_{m \in \mathbb{M}} C_m}{\sum_{m \in \mathbb{M}} (P_{m,p} + P_{\text{UAV-BS},m}) + P_{\text{gBS}} + P_{\text{AP}}}, \quad (52)$$

where $P_{m,p}$ is the source transmit power corresponds to UAV-BS m with aerial-passive-RIS, which also makes the backhaul rate $\{C_m\}_{m \in \mathbb{M}}$ for each UAV-BS m [43]. Thus, it is reasonable to compare $\sum_{m \in \mathbb{M}} P_{m,p}$ (in [43]) with obj for aerial-passive/active-RIS scenarios, respectively, which allows for a fair comparison of energy-efficiency minimization between the two cases. The simulation environment based on the parameters is illustrated in Fig. 3, and the detailed parameters are given in Table I.

B. Active-RIS vs. AF Relay: Performance Comparison

It is reasonable to explore the scenario where the aerial-active-RIS is not deployed. In such a case, an AF relay on the aerial platform serves as a natural alternative, as it similarly receives the incoming signal and forwards an amplified one to the destination. However, a closer comparison reveals that the proposed aerial-active-RIS architecture can offer greater advantages over the aerial-AF-relay. Specifically, the total AF-relay power consumption is expressed as [69]

$$\begin{aligned} P_{\text{tot,AF}} = & \sum_{m \in \mathbb{M}} (P_{m,\text{AF}} + P_{\text{UAV-BS},m}) + P_{\text{R,AF}} \\ & + P_{\text{gBS}} + P_{\text{circ,AF}} + P_{\text{AP}}, \end{aligned} \quad (53)$$

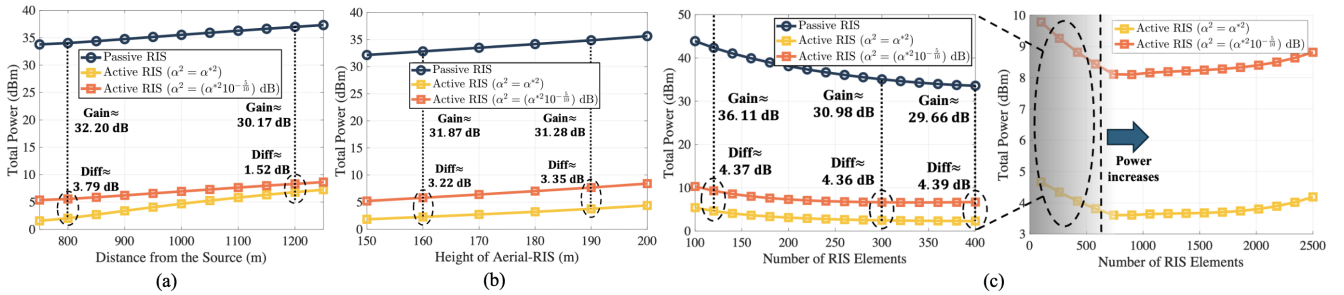


Fig. 7. Total power with respect to (a) the distance of ρ_G from the source (b) the height of aerial-RIS (c) the number of RIS elements under the implementation of proposed aerial-active-RIS with benchmarks.

where $\sum_{m \in \mathbb{M}} P_{m, \text{AF}}$ is the source transmit power needed to support the target rate, $P_{\text{R}, \text{AF}}$ is the relay transmit power (amplification power) required under the AF protocol, $P_{\text{circ}, \text{AF}}$ is hardware power cost of the N -element AF relay [69]:

$$P_{\text{circ}, \text{AF}} = N(P_{\text{DAC}} + P_{\text{mix}} + P_{\text{filt}}) + P_{\text{syn}}, \quad (54)$$

where P_{DAC} , P_{mix} , P_{filt} , and P_{syn} represent the power consumed by the digital-to-analog (DAC) converter, mixer, filter, and frequency synthesizer, respectively. Herein, same with the aerial-active-RIS, P_{AP} , P_{BS} and $\{P_{\text{UAV-BS}, m}\}_{m \in \mathbb{M}}$ are treated as constant offsets. According to practical values reported in [69], the combined term $P_{\text{DAC}} + P_{\text{mix}} + P_{\text{filt}}$ reaches approximately 18.2 dBm, which is over 20 dB higher than the corresponding P_E used in Table I. Furthermore, the additional contribution from P_{syn} further exacerbates the total power requirement. Although the aerial-AF-relay operates in full-duplex mode, it incurs additional hardware complexity to suppress self-interference [27], [70]. As a result, the aerial-AF-relay suffers from significantly higher power demands, particularly on the relay side, making it substantially less energy-efficient than the proposed aerial-active-RIS architecture.

For numerical comparison, Fig. 4 plots the resulting total power versus the distance of ρ_G from the source (d_G) for aerial-active-RIS vs. $N = M$ -element aerial-AF-relay [71]–[73]³ with optimal configuration employed by numerical exhaustive search. The figure shows that the aerial-AF-relay consistently requires substantially higher power, even with less number of elements ($M < N$ in general), than the aerial-active-RIS under identical throughput conditions: gain produced by 25.48 and 27.19 dB in $d_G = 1000$ and 1200 m, respectively. Note that beyond a certain distance in the figure, the AF-relay curve dramatically rises as the relay transmit power required to compensate for the multiplicative path loss becomes dominant [58]. Furthermore, the pronounced gap from aerial-active-RIS and aerial-AF-relay stems from the fundamental architectural differences between the two systems: the aerial-AF-relay incurs an additional relay transmission stage, where the aerial-AF-relay is located at an intermediate position between the source and the receivers, to compensate

for multiplicative path loss loss and amplified noise, together with a significantly larger RF-chain circuit power due to high-power components mentioned in (54), whereas the aerial-active-RIS benefits from cascaded source-RIS-destination reflection with amplification gain and relies only on low-power element-level amplification and control circuitry represented by P_E .

C. Reliability of Placement and Amplification in Aerial-Active-RIS

Fig. 5 illustrates the variation of κ_m with respect to the aerial-active-RIS height (H) and the 2D distance of the UAV-BS from the source ($\|\mathbf{w}_m\|_2$). It is observed that κ_m is on the order of 10^{-2} when $\|\mathbf{w}_m\|_2$ is sufficiently large, implying that $\mathbf{q}_m^* = \kappa_m \mathbf{w}_m$ lies extremely close to the origin relative to \mathbf{w}_m . Moreover, κ_m increases as H grows. This occurs because a larger H yields a greater a and a smaller $\sqrt{-\frac{a}{3}}$ (with $a < 0$) in (35), while the posterior term of $\sqrt{-\frac{a}{3}}$ in (35), approximated by $(-1 + \frac{\epsilon}{3\sqrt{3}})$ for $|\epsilon| \ll 1$ in (65), remains negative. Consequently, increasing H reduces $\sqrt{-\frac{a}{3}}$ and thereby enlarges κ_m . A similar analogy holds for decreasing $\|\mathbf{w}_m\|_2$, which likewise results in an increase of κ_m .

Fig. 6(a) and (b) show the behavior of α^{*2} according to H and $\|\mathbf{w}_m\|_2$, and the optimal total power (obj) with respect to α^2 with minimum at α^{*2} , respectively. As shown in (a), as H and $\|\mathbf{w}_m\|_2$ increase, α^{*2} exhibits a rising trend, which is clear since increase in H and $\|\mathbf{w}_m\|_2$ leads to farther link distance, which leads to stronger reflection compared to low H and $\|\mathbf{w}_m\|_2$. This also can be found in (71), where increase of H and $\|\mathbf{w}_m\|_2$ leads to the increase of $\sum_{m \in \mathbb{M}} \Omega_m \|\rho_{\text{RIS}}\|_2^2 \|\rho_{\text{RIS}} - \rho_m\|_2^2$. Moreover, we, in (b), can check the optimality of α^{*2} , where the global minimum can be achieved in α^{*2} with minimum total power given in obj and (69). Consequently, if α^{*2} exceeds the threshold of 40 dB, we select α^* by $\alpha^{*2} = 40$ dB as the optimum. From this point onward, we set $\alpha^2 = (\alpha^{*2} 10^{\frac{\Delta_0}{10}})$ dB as a reference for comparing the non-optimality with respect to $\alpha^2 = \alpha^{*2}$.

D. Comparison of Total Power under Various Conditions

Fig. 7(a) illustrates the total power according to the distance of ρ_G from the source (d_G) with the implementation of active-RIS. Here, the performance gain by our proposed algorithm

³Deploying an AF-relay with an antenna array whose size scales with N would imply hundreds of antenna elements, leading to prohibitive hardware cost and power consumption [69]. Consequently, the majority of the literature considers AF-relays whose antenna dimensions follow the scale of the TRx [71]–[73].

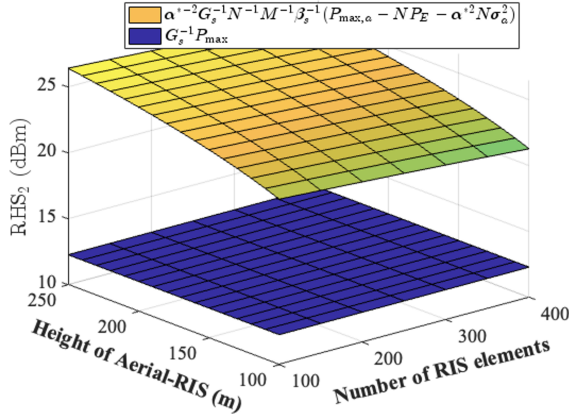


Fig. 8. Behavior of RHS_2 in (29) with respect to the height of aerial-RIS and the number of active-RIS elements.

with $\alpha^2 = \alpha^{*2}$ is approximately given by 32.20 and 30.17 dB for the distance 800 and 1200 m, respectively, which stably ensures almost 30 dB performance compared to total power of aerial-passive-RIS. It is also clear that d_G leads to the increase of total power, owing to the increase of path loss and probability to adopt the full-array scenario [43]. Moreover, as d_G increases, the power growth rate of the aerial-active-RIS becomes greater than that of the aerial-passive-RIS, which is shown by decrease in performance gain. It is because at longer distances, α^* becomes stronger, which also leads to an increase in both amplification power and dynamic noise which leads to the increase of total power.

We can also notice that the difference in total power between $\alpha^2 = \alpha^{*2}$ and $(\alpha^{*2} 10^{\frac{\Delta_0}{10}})$ dB with $\Delta_0 = -5$ decreases from 3.79 to 1.52 dB for the distance of 800 to 1200 m, respectively, which implies the dependence on α near α^* decreases when d_G increases. We can analyze this phenomenon by taking the natural log of (69) by $p(\alpha)$ (i.e., $p(\alpha) = \ln(\text{obj})$), and considering

$$p(\alpha^*(1 + \epsilon)) - p(\alpha^*)^4 \quad (55)$$

for small ϵ .⁵ It is evident that a smaller value of (55) indicates a weaker sensitivity to α in the vicinity of α^* , in terms of dB.

Hence, by directly computing (55) we can get (56). From (56), it is clear that as d_G increases, $\|\rho_{\text{RIS}} - \rho_m\|_2^2$ also increases, causing the RHS of (56) to approach 0. Conversely, when d_G decreases, the argument inside the logarithm approaches $\frac{1}{2} \left((1 + \epsilon)^2 + (1 + \epsilon)^{-2} \right) > 1$. Therefore, we can conclude that an increase in d_G implies a reduced dependency on α in dB for the total power in dBm.

Fig. 7(b) illustrates the total power according to feasible H with the guarantee of high LoS probability [7], [8]. Clearly, by applying our algorithm with $\alpha^2 = \alpha^{*2}$, for increase of $H = 160$ to 190 m, we can reduce the total power by

⁴The power is measured in dBm, and we consider the variation of α in dB.

⁵Although ϵ is small, the product α can be significant due to the scale of α , as shown in Fig. 6. Therefore, approximations such as using Taylor's first order expansion to estimate the difference are not reliable in this context. Instead, the total power difference in dBm should be computed directly.

approximately 31.87 and 31.28 dB, respectively, compared to the passive-RIS-equipped benchmark algorithms. Similar to the scenario illustrated in Fig. 7, an increase in H results in a greater distance between the UAV-BS and the aerial-RIS, which leads to, similar to Fig. 7, the decrease of performance gain. Furthermore, by applying the same reasoning to the RHS of (56), and noting that $\|\rho_{\text{RIS}}\|_2^2, \|\rho_{\text{RIS}} - \rho_m\|_2^2 \sim \mathcal{O}(H^2)$, it follows that both the numerator and denominator of the RHS of (56) scale as $\mathcal{O}(H^2)$, which implies that the RHS of (56) scales as $\mathcal{O}(1)$ with respect to H . This indicates that the variation in total power, measured in dBm, with respect to α in dB remains nearly constant with increasing H , which is also shown in Fig. 7(b).

Fig. 7(c) shows the total power with respect to the number of active-RIS elements (N). Note that in particular, the N -dependent circuit-related term appears as $(\alpha^2 \sigma_a^2 + P_E)N$, whereas the remaining dominant terms in obj scale as $\mathcal{O}(1)$ with respect to N [43]. As a result, we can observe that the power increases in large scale of N . Nevertheless, the RIS is modeled as a ULA, to avoid illustrating unrealistic regimes with excessively large arrays, we therefore restrict N to a feasible range, which is the left-side of Fig. 7(c). As shown in the figure, although considering the reflection power P_R and power consumption by active hardware $N P_E$, the proposed method with aerial-active-RIS greatly reduces the power, where the performance gain by our proposed algorithm with $\alpha^2 = \alpha^{*2}$ is approximately given by 36.11 and 30.98 dB for $N = 120$ and 300, respectively. In addition, we can notice that the difference of total power in dB between passive and active-RIS scenario is in first (small N) large enough, and gradually gets smaller in given range of the number of RIS elements. It is because when N is small, obj is asymptotically $\text{obj} \sim \sum_{m \in \mathbb{M}} P_m$, and by applying $N \rightarrow 0$ to (25), P_m goes to $\alpha^{-2} P_{m,p}$ [43]. By combining those aspects, it is clear that the total power gain between aerial-active- and passive-RIS goes to α^2 , and by increasing N , the impact of the dynamic noise $\alpha^2 N \sigma_a^2$, the active-RIS-reflection power $\alpha^2 N M \beta_s G_s \sum_{m \in \mathbb{M}} P_m$, and the active-circuit-dissipated power $N P_E$ is added to $\sum_{m \in \mathbb{M}} P_m$ and formulate obj, affects to the increase of total power in combined way and the gain is becoming less than α^2 . Furthermore, both the numerator and the denominator of RHS of (56) scales as $\mathcal{O}(\sqrt{(N + N^2 g^{-1}) g^{-1}} + N g^{-1} + N)$, which also implies that (56) scales with $\mathcal{O}(1)$ with respect to N . This suggests that the total power perturbation from α^* to $\alpha^* + d$ in dBm stays constant with N , as illustrated in Fig. 7(c).

Fig. 8 shows the behavior of RHS_2 in (29), which is the upper-bound of source transmit power $\sum_{m \in \mathbb{M}} P_m$. From the given figure, the expression

$$\alpha^{*-2} G_s^{-1} N^{-1} M^{-1} \beta_s^{-1} (P_{\text{max},a} - N P_E - \alpha^{*2} N \sigma_a^2) \quad (57)$$

in RHS_2 decreases as H and N decrease, where the reduction is primarily due to the term $N^{-1} \beta_s^{-1}$. Meanwhile, the term $G_s^{-1} P_{\text{max}}$ remains nearly constant, as it is almost a constant under the assumption that the antenna beamforming at the ground backhaul source is almost perfectly aligned with the aerial-active-RIS [74]–[76]. Moreover, the upper-bound is observed to be in range of 12~15 dBm. Meanwhile, the total

$$\begin{aligned}
& p(\alpha^*(1+\epsilon)) - p(\alpha^*) \\
&= \ln \left(\frac{\left((1+\epsilon)^2 + (1+\epsilon)^{-2} \right) \sqrt{\left(N\sigma_a^2 + \sum_{m \in \mathbb{M}} \Omega_0 \Omega_1 \Omega_2 \right) \left(\sum_{m \in \mathbb{M}} \Omega_0 \|\boldsymbol{\rho}_{\text{RIS}}\|_2^2 \|\boldsymbol{\rho}_{\text{RIS}} - \boldsymbol{\rho}_m\|_2^2 \right)} + \sum_{m \in \mathbb{M}} \left(\Omega_0 \|\boldsymbol{\rho}_{\text{RIS}}\|_2^2 \Omega_2 + \Omega_0 \|\boldsymbol{\rho}_{\text{RIS}} - \boldsymbol{\rho}_m\|_2^2 \Omega_1 \right) + NP_E}{2 \sqrt{\left(N\sigma_a^2 + \sum_{m \in \mathbb{M}} \Omega_0 \Omega_1 \Omega_2 \right) \left(\sum_{m \in \mathbb{M}} \Omega_0 \|\boldsymbol{\rho}_{\text{RIS}}\|_2^2 \|\boldsymbol{\rho}_{\text{RIS}} - \boldsymbol{\rho}_m\|_2^2 \right)} + \sum_{m \in \mathbb{M}} \left(\Omega_0 \|\boldsymbol{\rho}_{\text{RIS}}\|_2^2 \Omega_2 + \Omega_0 \|\boldsymbol{\rho}_{\text{RIS}} - \boldsymbol{\rho}_m\|_2^2 \Omega_1 \right) + NP_E} \right) \quad (56)
\end{aligned}$$

power in the simulations (obj), presented in Fig. 7(a)~(c), almost surely remains below 10 dBm, which is strictly larger than the source transmit power:

$$\begin{aligned}
\text{obj} &\triangleq (1 + \alpha^2 NM \beta_s G_s) \sum_{m \in \mathbb{M}} P_m + \alpha^2 N \sigma_a^2 + NP_E \\
&> \sum_{m \in \mathbb{M}} P_m.
\end{aligned} \quad (58)$$

Hence, we can observe that it leads to the fact that $\sum_{m \in \mathbb{M}} P_m$ also stays below 10 dBm, which does not exceed the RHS₂ that are computed in Fig. 8. This equivalently indicates that the proposed system remains within the feasible region defined by RHS₂ in (29).

V. CONCLUSION

In this paper, we proposed a novel aerial-active-RIS-assisted backhaul architecture to enable energy-efficient full 3D coverage for UAV-BS backhaul networks in 6G. We derived the minimum total power required for backhauling UAV-BSs under target data rate constraints and showed that equal amplification gain is an effective strategy for maximizing energy-efficiency. By employing a practical aerial-active-RIS signal model and accounting for active-RIS-induced dynamic noise, we optimized the placement, array configuration, amplification gain, and phase of the aerial-active-RIS. Simulation results validated the effectiveness of the proposed method, demonstrating significant energy-efficiency improvements over benchmarks and highlighting its strong potential for delivering reliable and scalable 3D backhaul coverage in 6G.

APPENDIX A

PROOF OF THEOREM 1

Let $\bar{\mathbf{q}}_m$ be the orthogonal projection of \mathbf{q}_m onto the line segment connecting the source and \mathbf{w}_m . Thereafter, the following holds:

$$\begin{cases} \|\mathbf{q}_m - \mathbf{w}_m\|_2^2 = \|\mathbf{q}_m - \bar{\mathbf{q}}_m\|_2^2 + \|\bar{\mathbf{q}}_m - \mathbf{w}_m\|_2^2 \\ \|\mathbf{q}_m\|_2^2 = \|\mathbf{q}_m - \bar{\mathbf{q}}_m\|_2^2 + \|\bar{\mathbf{q}}_m\|_2^2 \end{cases} \quad (59)$$

To minimize the objective in (33), it is necessary to minimize the left-hand side in (59). Consequently, \mathbf{q}_m should satisfy:

$$\|\mathbf{q}_m - \bar{\mathbf{q}}_m\|_2^2 = 0 \Leftrightarrow \mathbf{q}_m = \kappa_m \mathbf{w}_m \quad (\kappa_m > 0), \quad (60)$$

which is clarified in Fig. 9. Hence, by substituting (60) we

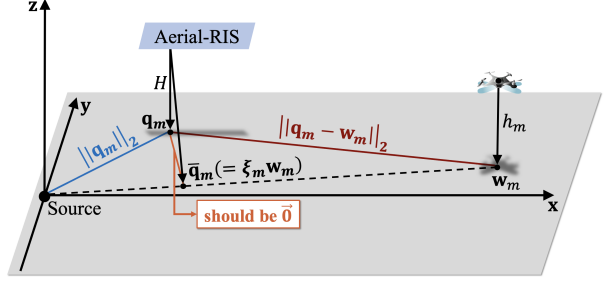


Fig. 9. Illustration of (60) in Theorem 1: orthogonal projection of \mathbf{q}_m .

can denote the objective of (33) by $g(\kappa_m)$, that is:

$$g(\kappa_m) \triangleq \|\mathbf{w}_m\|_2^4 (\kappa_m^2 + \zeta_1^2 + \bar{\Omega}_1) \left((1 - \kappa_m)^2 + \zeta_2^2 + \bar{\Omega}_2 \right), \quad (61)$$

where

$$\zeta_1 = \frac{H}{\|\mathbf{w}_m\|_2}, \zeta_2 = \frac{|H - h_m|}{\|\mathbf{w}_m\|_2}, \bar{\Omega}_i = \|\mathbf{w}_m\|_2^{-2} \tilde{\Omega}_i \quad (i = 1, 2). \quad (62)$$

To find the minimum of g at $\kappa_m > 0$, we have to solve $g'(\kappa_m) = 0$. The discriminant Δ of the cubic equation $g'(\kappa_m) = 0$ is given by $\Delta = \left(\frac{a}{3}\right)^3 + \left(\frac{b}{2}\right)^2$ [77], where $a = \frac{1}{2}(\zeta_1^2 + \zeta_2^2 + \bar{\Omega}_1 + \bar{\Omega}_2) - \frac{1}{4}$, $b = \frac{1}{4}(\zeta_2^2 - \zeta_1^2 + \bar{\Omega}_2 - \bar{\Omega}_1)$. For the range of a and b , we can assume the followings:

- 1) Since we assume that d_G is sufficiently large, $\|\mathbf{w}_m\|_2$ follows a similar scale. In this paper, we will assume the scale with 10^3 m, which is also reflected in the simulation in Section IV and Table I.
- 2) $\beta_0 \approx -43.3$ dB for sub-6 GHz backhaul (gets larger for higher-frequency applications in 6G [17], [78], [79]).
- 3) Feasible α_{\max}^2 is given by less than 40 dB [27], [28].
- 4) $G_s \leq G_{\max} = 8$ dB in Table I.
- 5) We assume that M and N has a scale of approximately a few or less than ten and few hundred, respectively: $M = 16, N \in [100, 400]$ [27], [43], [58]
- 6) σ_a^2 and σ^2 has the similar scale [28], [32].

Therefore, we can assume that

$$\zeta_i \ll 1 \quad (i = 1, 2)$$

$$\bar{\Omega}_1 = \alpha^2 NM \beta_0 G_s \|\mathbf{w}\|_2^{-2} \ll 1, \quad \bar{\Omega}_2 = \alpha^2 \frac{\sigma_a^2}{\sigma^2} N \beta_0 \|\mathbf{w}_m\|_2^{-2} \ll 1, \quad (63)$$

which also leads to $a < 0$ ($\approx -\frac{1}{4}$) and $|b| \ll 1$. Hence, we can deduce $\Delta < 0$, which leads to three real solutions $\{\kappa_{m,k}\}_{k=0}^2$ of $g'(\kappa_m) = 0$ [77]:

$$\kappa_{m,k} = \frac{1}{2} + 2\sqrt{-\frac{a}{3}} \cos \left(\frac{1}{3} \cos^{-1} \left(\frac{3b}{2a} \sqrt{-\frac{3}{a}} \right) - \frac{2}{3}\pi k \right) \quad (k = 0, 1, 2). \quad (64)$$

Since $a \approx -\frac{1}{4}$ and $|b| \ll 1$, we define $\frac{3b}{2a} \sqrt{-\frac{3}{a}} = \epsilon$ with $|\epsilon| \ll 1$. By successively applying the first-order Taylor approximation to (64), the expression reduces to

$$\begin{cases} \kappa_{m,0} \approx \frac{1}{2} + \sqrt{-a} \left(1 + \frac{\epsilon}{3\sqrt{3}} \right) \\ \kappa_{m,1} \approx \frac{1}{2} + \sqrt{-a} \left(-\frac{\epsilon}{3\sqrt{3}} \right) \\ \kappa_{m,2} \approx \frac{1}{2} + \sqrt{-a} \left(-1 + \frac{\epsilon}{3\sqrt{3}} \right). \end{cases} \quad (65)$$

By substituting $a = \frac{1}{2}(\zeta_1^2 + \zeta_2^2 + \bar{\Omega}_1 + \bar{\Omega}_2) - \frac{1}{4}$, (65) becomes

$$\begin{cases} \kappa_{m,0} \approx \frac{1}{2} - \sqrt{\frac{1}{4} - \frac{1}{2}(\zeta_1^2 + \zeta_2^2 + \bar{\Omega}_1 + \bar{\Omega}_2)} \left(-1 - \frac{\epsilon}{3\sqrt{3}} \right) \\ \kappa_{m,1} \approx \frac{1}{2} - \sqrt{\frac{1}{4} - \frac{1}{2}(\zeta_1^2 + \zeta_2^2 + \bar{\Omega}_1 + \bar{\Omega}_2)} \left(\frac{\epsilon}{3\sqrt{3}} \right) \\ \kappa_{m,2} \approx \frac{1}{2} - \sqrt{\frac{1}{4} - \frac{1}{2}(\zeta_1^2 + \zeta_2^2 + \bar{\Omega}_1 + \bar{\Omega}_2)} \left(1 - \frac{\epsilon}{3\sqrt{3}} \right). \end{cases} \quad (66)$$

From (66), we can derive the following outcomes:

- 1) It is evident that $\kappa_{m,0} > \kappa_{m,1} > \kappa_{m,2}$ ($\because |\epsilon| \ll 1$).
- 2) By the properties of the quartic equation [77], g has two local minimum: $\kappa_{m,0}$ and $\kappa_{m,2}$, with one of them being the global minimum.
- 3) Using $|\epsilon| \ll 1$, we can deduce the following for $\kappa_{m,2}$:

$$\begin{aligned} \kappa_{m,2} &\approx \frac{1}{2} - \sqrt{\frac{1}{4} - \frac{1}{2}(\zeta_1^2 + \zeta_2^2 + \bar{\Omega}_1 + \bar{\Omega}_2)} (1) \\ &= \frac{\frac{1}{2}(\zeta_1^2 + \zeta_2^2 + \bar{\Omega}_1 + \bar{\Omega}_2)}{\sqrt{\frac{1}{4} + \frac{1}{2}(\zeta_1^2 + \zeta_2^2 + \bar{\Omega}_1 + \bar{\Omega}_2)}} > 0. \end{aligned} \quad (67)$$

Furthermore, as ζ_1 and ζ_2 are sufficiently small (owing to the sufficiently large $\|\mathbf{w}_m\|_2$), it follows from (67) that $\kappa_{m,2}$ should be close to the origin.

Hence, we should select κ_m as

$$\begin{aligned} \kappa_m &\stackrel{\Delta}{=} \kappa_{m,2} \\ &= \frac{1}{2} + 2\sqrt{-\frac{a}{3}} \cos \left(\frac{1}{3} \cos^{-1} \left(\frac{3b}{2a} \sqrt{-\frac{3}{a}} \right) - \frac{4}{3}\pi \right). \end{aligned} \quad (68)$$

By determining $\mathbf{q}_m^* = \kappa_m \mathbf{w}_m$ accordingly, the theorem follows. ■

APPENDIX B PROOF OF THEOREM 2

For given $\mathbf{q}^*, \{\bar{N}\}, \bar{\rho}$ (or $\{\bar{\rho}_i^*\}_{i=1}^L, \Theta$, obj in (29) becomes

$$\begin{aligned} &(1 + \alpha^2 NM\beta_s G_s) \sum_{m \in \mathbb{M}} P_m + \alpha^2 N\sigma_a^2 + NP_E (\triangleq \text{obj}) \\ &= \left(N\sigma_a^2 + \sum_{m \in \mathbb{M}} \Omega_0 \Omega_1 \Omega_2 \right) \alpha^2 \\ &\quad + \left(\sum_{m \in \mathbb{M}} \Omega_0 \|\boldsymbol{\rho}_{\text{RIS}}\|_2^2 \|\boldsymbol{\rho}_{\text{RIS}} - \boldsymbol{\rho}_m\|_2^2 \right) \alpha^{-2} \\ &\quad + \sum_{m \in \mathbb{M}} \left(\Omega_0 \|\boldsymbol{\rho}_{\text{RIS}}\|_2^2 \Omega_2 + \Omega_0 \|\boldsymbol{\rho}_{\text{RIS}} - \boldsymbol{\rho}_m\|_2^2 \Omega_1 \right) + NP_E, \end{aligned} \quad (69)$$

Hence, we can derive the optimal α by applying the Arithmetic-Geometric Mean inequality, which becomes (70). Therefore, by the equality condition of (70), we can deduce the optimal α^* as

$$\alpha^* = \min \left\{ \sqrt[4]{\frac{\sum_{m \in \mathbb{M}} \Omega_0 \|\boldsymbol{\rho}_{\text{RIS}}\|_2^2 \|\boldsymbol{\rho}_{\text{RIS}} - \boldsymbol{\rho}_m\|_2^2}{N\sigma_a^2 + \sum_{m \in \mathbb{M}} \Omega_0 \Omega_1 \Omega_2}}, \alpha_{\max} \right\}, \quad (71)$$

and the theorem follows. ■

REFERENCES

- [1] H.-B. Jeon and C.-B. Chae, "Energy-efficient aerial-RIS deployment for 6G," in *Proc. IEEE Int. Conf. ICT Converg. (ICTC)*, 2022, pp. 199–201.
- [2] B. Smida *et al.*, "Full-duplex wireless for 6G: Progress brings new opportunities and challenges," *IEEE J. Sel. Areas Commun.*, vol. 41, no. 9, pp. 2729–2750, Sep. 2023.
- [3] E. Björnson *et al.*, "Towards 6G MIMO: Massive spatial multiplexing, dense arrays, and interplay between electromagnetics and processing," *arXiv:2401.02844v1*, 2024.
- [4] Y. Kim *et al.*, "A state-of-the-art survey on full-duplex network design," *Proc. IEEE*, vol. 112, no. 5, pp. 463–486, May 2024.
- [5] M. Giordani and M. Zorzi, "Non-terrestrial networks in the 6G era: Challenges and opportunities," *IEEE Netw.*, vol. 35, no. 2, pp. 244–251, Mar./Apr. 2021.
- [6] M. Mozaffari *et al.*, "A tutorial on UAVs for wireless networks: Applications, challenges, and open problems," *IEEE Commun. Surveys Tuts.*, vol. 21, no. 3, pp. 2334–2360, Third quarter 2019.
- [7] A. Al-Hourani *et al.*, "Modeling air-to-ground path loss for low altitude platforms in urban environments," in *Proc. IEEE Glob. Commun. Conf. (GLOBECOM) Workshops*, Dec. 2014, pp. 2898–2904.
- [8] S.-C. Noh *et al.*, "Energy-efficient deployment of multiple UAVs using ellipse clustering to establish base stations," *IEEE Wireless Commun. Lett.*, vol. 9, no. 8, pp. 1155–1159, Aug. 2020.
- [9] Y. Zhang *et al.*, "Deployment optimization of tethered drone-assisted integrated access and backhaul networks," *IEEE Trans. Wireless Commun.*, vol. 23, no. 4, pp. 2668–2680, Apr. 2024.
- [10] C. Diaz-Vilas *et al.*, "Cell-free UAV networks: Asymptotic analysis and deployment optimization," *IEEE Trans. Wireless Commun.*, vol. 22, no. 5, pp. 3055–3070, May 2023.
- [11] H.-J. Moon *et al.*, "A generalized pointing error model for FSO links with fixed-wing UAVs for 6G: Analysis and trajectory optimization," *IEEE Trans. Wireless Commun.*, vol. 24, no. 7, pp. 5723–5737, Jul. 2025.
- [12] X. Guan *et al.*, "3D trajectory optimization for fixed-wing UAV communications with full UAV dynamics," *IEEE Trans. Veh. Technol.*, vol. 74, no. 10, pp. 15401–15415, 2025.
- [13] H.-J. Moon and C.-B. Chae, "Cooperative ground-satellite scheduling and power allocation for urban air mobility networks," *IEEE J. Sel. Areas Commun.*, vol. 43, no. 1, pp. 218–233, Jan. 2025.
- [14] H. Xiao *et al.*, "Energy-efficient STAR-RIS enhanced UAV-enabled MEC networks with bi-directional task offloading," *IEEE Trans. Wireless Commun.*, vol. 24, no. 4, pp. 3258–3272, Apr. 2025.

$$\begin{aligned}
& (1 + \alpha^2 NM \beta_s G_s) \sum_{m \in \mathbb{M}} P_m + \alpha^2 N \sigma_a^2 + N P_E \\
& \geq 2 \sqrt{\left(N \sigma_a^2 + \sum_{m \in \mathbb{M}} \Omega_0 \Omega_1 \Omega_2 \right) \left(\sum_{m \in \mathbb{M}} \Omega_0 \|\boldsymbol{\rho}_{\text{RIS}}\|_2^2 \|\boldsymbol{\rho}_{\text{RIS}} - \boldsymbol{\rho}_m\|_2^2 \right) + \sum_{m \in \mathbb{M}} \left(\Omega_0 \|\boldsymbol{\rho}_{\text{RIS}}\|_2^2 \Omega_2 + \Omega_0 \|\boldsymbol{\rho}_{\text{RIS}} - \boldsymbol{\rho}_m\|_2^2 \Omega_1 \right)} + N P_E.
\end{aligned} \tag{70}$$

[15] H.-B. Jeon *et al.*, “Free-space optical communications for 6G wireless networks: Challenges, opportunities, and prototype validation,” *IEEE Commun. Mag.*, vol. 61, no. 4, pp. 116–121, Apr. 2023.

[16] Y. Kim *et al.*, “Low complexity frequency domain nonlinear self-interference cancellation for flexible duplex,” *IEEE Trans. Wireless Commun.*, vol. 24, no. 8, pp. 6627–6642, Aug. 2025.

[17] D. Jun *et al.*, “Reconfigurable intelligence surface with potential tunable meta-devices for 6G: Design and system-level evaluation,” *IEEE Commun. Stand. Mag.*, vol. 8, no. 4, pp. 32–39, Apr. 2024.

[18] Q. Wu *et al.*, “Intelligent reflecting surface-aided wireless communications: A tutorial,” *IEEE Trans. Commun.*, vol. 69, no. 5, pp. 3313–3351, May 2021.

[19] E. Basar and H. V. Poor, “Present and future of reconfigurable intelligent surface-empowered communications [perspectives],” *IEEE Signal Process. Mag.*, vol. 38, no. 6, pp. 146–152, Nov. 2021.

[20] Y. Liu *et al.*, “Reconfigurable intelligent surfaces: Principles and opportunities,” *IEEE Communications Surveys & Tutorials*, vol. 23, no. 3, pp. 1546–1577, Third Quarter 2021.

[21] L. Dai *et al.*, “Reconfigurable intelligent surface-based wireless communications: Antenna design, prototyping, and experimental results,” *IEEE Access*, vol. 8, pp. 45 913–45 923, 2020.

[22] J. Sang *et al.*, “Coverage enhancement by deploying RIS in 5G commercial mobile networks: Field trials,” *IEEE Wireless Commun.*, vol. 31, no. 1, pp. 172–180, Feb. 2024.

[23] —, “Multi-scenario broadband channel measurement and modeling for sub-6 GHz RIS-assisted wireless communication systems,” *IEEE Trans. Wireless Commun.*, vol. 23, no. 6, pp. 6312–6329, Jun. 2024.

[24] E. Björnson *et al.*, “Intelligent reflecting surface versus decode-and-forward: How large surfaces are needed to beat relaying?” *IEEE Wireless Commun. Lett.*, vol. 9, no. 2, pp. 244–248, Feb. 2020.

[25] M. Di Renzo *et al.*, “Reconfigurable intelligent surfaces vs. relaying: Differences, similarities, and performance comparison,” *IEEE Open J. Commun. Soc.*, vol. 1, pp. 798–807, Jun. 2020.

[26] H. Do and N. Lee, “Finding globally optimal configuration of active RIS in linear time,” *IEEE Trans. Wireless Commun.*, vol. 23, no. 12, pp. 18 142–18 153, Dec. 2024.

[27] Z. Zhang *et al.*, “Active RIS vs. passive RIS: Which will prevail in 6G?” *IEEE Trans. Commun.*, vol. 71, no. 3, pp. 1707–1725, Mar. 2023.

[28] K. Zhi *et al.*, “Active RIS versus passive RIS: Which is superior with the same power budget?” *IEEE Commun. Lett.*, vol. 26, no. 5, pp. 1150–1154, May 2022.

[29] M. Ahmed *et al.*, “Active reconfigurable intelligent surfaces: Expanding the frontiers of wireless communication—a survey,” *IEEE Commun. Surveys Tuts.*, vol. 27, no. 2, pp. 839–869, Apr. 2025.

[30] G. C. Alexandropoulos *et al.*, “Reconfigurable intelligent surfaces for rich scattering wireless communications: Recent experiments, challenges, and opportunities,” *IEEE Commun. Mag.*, vol. 59, no. 6, pp. 28–34, Jun. 2021.

[31] Q. Zhu *et al.*, “Joint beamforming designs for active reconfigurable intelligent surface: A sub-connected array architecture,” *IEEE Trans. Commun.*, vol. 70, no. 11, pp. 7628–7643, Nov. 2022.

[32] R. Long *et al.*, “Active reconfigurable intelligent surface-aided wireless communications,” *IEEE Trans. Wireless Commun.*, vol. 20, no. 8, pp. 4962–4975, Aug. 2021.

[33] G. Zhou *et al.*, “A framework for transmission design for active RIS-aided communication with partial CSI,” *IEEE Trans. Wireless Commun.*, vol. 23, no. 1, pp. 305–320, Jan. 2024.

[34] J. Yang *et al.*, “Robust transmission design for active RIS-aided systems,” *IEEE Trans. Veh. Technol.*, pp. 1–6, 2025.

[35] J. Liu and H. Zhang, “Throughput optimization in aerial RIS-assisted networks with 3D imperfect reflection,” *IEEE Trans. Veh. Technol.*, vol. 74, no. 7, pp. 10 510–10 523, Jul. 2025.

[36] H. Lu *et al.*, “Aerial intelligent reflecting surface: Joint placement and passive beamforming design with 3D beam flattening,” *IEEE Trans. Wireless Commun.*, vol. 20, no. 7, pp. 4128–4143, Jul. 2021.

[37] B. Xiong *et al.*, “Performance analysis of aerial RIS auxiliary mmWave mobile communications with UAV fluctuation,” *IEEE Wireless Commun. Lett.*, vol. 13, no. 4, pp. 1183–1187, Apr. 2024.

[38] S. Faramarzi *et al.*, “Meta reinforcement learning for resource allocation in aerial active-RIS-assisted networks with rate-splitting multiple access,” *IEEE Internet Things J.*, vol. 11, no. 15, pp. 26 366–26 383, Aug. 2024.

[39] J. Zhao *et al.*, “Aerial active STAR-RIS-aided IoT NOMA networks,” *IEEE Internet Things J.*, vol. 12, no. 8, pp. 9525–9538, Apr. 2025.

[40] D. Wang *et al.*, “Active aerial reconfigurable intelligent surface assisted secure communications: Integrating sensing and positioning,” *IEEE J. Sel. Areas Commun.*, vol. 42, no. 10, pp. 2769–2785, Oct. 2024.

[41] M. Toka *et al.*, “RIS-empowered LEO satellite networks for 6G: Promising usage scenarios and future directions,” *IEEE Commun. Mag.*, vol. 62, no. 11, pp. 128–135, Nov. 2024.

[42] C. A. Balanis, *Antenna Theory: Analysis and Design*. New York, NY, USA: Wiley, 2016.

[43] H.-B. Jeon *et al.*, “An energy-efficient aerial backhaul system with reconfigurable intelligent surface,” *IEEE Trans. Wireless Commun.*, vol. 21, no. 8, pp. 6478–6494, Aug. 2022.

[44] J. Lei *et al.*, “NOMA for STAR-RIS assisted UAV networks,” *IEEE Trans. Commun.*, vol. 72, no. 3, pp. 1732–1745, Mar. 2024.

[45] N. Gao and ohters, “Aerial RIS-assisted high altitude platform communications,” *IEEE Wireless Commun. Lett.*, vol. 10, no. 10, pp. 2096–2100, Oct. 2021.

[46] H. Lu *et al.*, “Enabling panoramic full-angle reflection via aerial intelligent reflecting surface,” in *Proc. IEEE Int. Conf. on Comm. (ICC) Workshops*, 2020, pp. 1–6.

[47] X. Yu *et al.*, “Channel estimation for irregular subarrayed RIS-aided mmWave communications,” *IEEE Trans. Veh. Technol.*, vol. 74, no. 11, pp. 17 247–17 264, Nov. 2025.

[48] S. Chen *et al.*, “Interference suppression for active RIS-empowered array radar using joint beamforming design,” *IEEE Trans. Veh. Technol.*, vol. 74, no. 4, pp. 6222–6238, Apr. 2025.

[49] ITU-R P.525-2, “Calculation of free-space attenuation,” 1994.

[50] L. Wei *et al.*, “Channel estimation for RIS-empowered multi-user MISO wireless communications,” *IEEE Trans. Commun.*, vol. 69, no. 6, pp. 4144–4157, Jun. 2021.

[51] J. Chen *et al.*, “Channel estimation for reconfigurable intelligent surface aided multi-user mmWave MIMO systems,” *IEEE Trans. Wireless Commun.*, vol. 22, no. 10, pp. 6853–6869, Oct. 2023.

[52] X. Wei *et al.*, “Channel estimation for RIS assisted wireless communications—Part II: An improved solution based on double-structured sparsity,” *IEEE Commun. Lett.*, vol. 25, no. 5, pp. 1403–1407, May 2021.

[53] G. Zhou *et al.*, “Individual channel estimation for RIS-aided communication systems—a general framework,” *IEEE Trans. Wireless Commun.*, vol. 23, no. 9, pp. 12 038–12 053, Sep. 2024.

[54] K. Liu *et al.*, “Active reconfigurable intelligent surface: Fully-connected or sub-connected?” *IEEE Commun. Lett.*, vol. 26, no. 1, pp. 167–171, Jan. 2022.

[55] H. Niu *et al.*, “Active RIS assisted rate-splitting multiple access network: Spectral and energy efficiency tradeoff,” *IEEE J. Sel. Areas Commun.*, vol. 41, no. 5, pp. 1452–1467, May 2023.

[56] R. C. Hansen, *Phased Array Antennas*. Hoboken, NJ, USA: John Wiley & Sons, 2009.

[57] *Study on new radio access technology: Radio access architecture and interfaces*. document 3GPP TR 38.801, Jan. 2016.

[58] C. Huang *et al.*, “Reconfigurable intelligent surfaces for energy efficiency in wireless communication,” *IEEE Trans. Wireless Commun.*, vol. 18, no. 8, pp. 4157–4170, Aug. 2019.

[59] J.-F. Bousquet *et al.*, “A 4-GHz active scatterer in 130-nm CMOS for phase sweep amplify-and-forward,” *IEEE Trans. Circuits Syst. I, Reg. Papers*, vol. 59, no. 3, pp. 529–540, Mar. 2012.

- [60] F. Amato, C. W. Peterson, B. P. Degnan, and G. D. Durgin, "Tunneling RFID tags for long-range and low-power microwave applications," *IEEE J. Radio Freq. Identificat.*, vol. 2, no. 2, pp. 93–103, Jun. 2018.
- [61] Y. Zeng *et al.*, "Energy minimization for wireless communication with rotary-wing UAV," *IEEE Trans. Wireless Commun.*, vol. 18, no. 4, pp. 2329–2345, April 2019.
- [62] K. Miettinen, *Nonlinear Multiobjective Optimization*. Dordrecht, Netherlands: Kluwer Academic Publishers, 1998.
- [63] E. Weiszfeld and F. Plastria, "On the point for which the sum of the distances to n given points is minimum," *Ann. Oper. Res.*, vol. 167, no. 1, pp. 7–41, Mar. 2009.
- [64] A. Beck and S. Sabach, "Weiszfeld's method: Old and new results," *J. Optim. Theory Appl.*, vol. 164, no. 1, pp. 1–40, May 2015.
- [65] S. Boyd and L. Vandenberghe, *Convex Optimization*. Cambridge, UK: Cambridge Univ. Press, 2004.
- [66] A. Zappone and E. Jorswieck, "Energy efficiency in wireless networks via fractional programming theory," *Found. Trends Commun. Inf. Theory*, vol. 11, no. 3-4, pp. 185–396, 2015.
- [67] C. Liaskos *et al.*, "A new wireless communication paradigm through software-controlled metasurfaces," *IEEE Commun. Mag.*, vol. 56, no. 9, pp. 162–169, Sep. 2018.
- [68] *Study on Channel Model for Frequencies From 0.5 to 100 GHz*. document 3GPP TR 38.901, Jan. 2020.
- [69] H. Kim *et al.*, "A cross-layer approach to energy efficiency for adaptive MIMO systems exploiting spare capacity," *IEEE Trans. Wireless Commun.*, vol. 8, no. 8, pp. 4264–4275, Aug. 2009.
- [70] K. Nontanin *et al.*, "Multi-antenna relaying and reconfigurable intelligent surfaces: End-to-end SNR and achievable rate," *arXiv:1908.07967v2*, 2019.
- [71] A. Zappone *et al.*, "Energy efficiency optimization in relay-assisted MIMO systems with perfect and statistical CSI," *IEEE Trans. Signal Process.*, vol. 62, no. 2, pp. 443–457, Jan. 2014.
- [72] B. Sainath and N. B. Mehta, "Generalizing the amplify-and-forward relay gain model: An optimal SEP perspective," *IEEE Trans. Wireless Commun.*, vol. 11, no. 11, pp. 4118–4127, Nov. 2012.
- [73] C.-B. Chae *et al.*, "MIMO relaying with linear processing for multiuser transmission in fixed relay networks," *IEEE Trans. Signal Process.*, vol. 56, no. 2, pp. 727–738, Feb. 2008.
- [74] K. Liang *et al.*, "A data and model-driven deep learning approach to robust downlink beamforming optimization," *IEEE J. Sel. Areas Commun.*, vol. 42, no. 11, pp. 3278–3292, Nov. 2024.
- [75] M. S. Sim *et al.*, "Deep learning-based mmWave beam selection for 5G NR/6G with sub-6 GHz channel information: Algorithms and prototype validation," *IEEE Access*, vol. 8, pp. 51 634–51 646, 2020.
- [76] Q. Deng *et al.*, "Adaptive beam alignment and optimization for IRS-aided high-speed UAV communications," *IEEE Trans. Green Commun. Netw.*, vol. 7, no. 3, pp. 1583–1595, Oct. 2023.
- [77] S. Lovett, *Abstract Algebra: Structures and Applications*. Boca Raton, FL, USA: CRC Press, 2015.
- [78] M. R. Castellanos *et al.*, "Embracing reconfigurable antennas in the tri-hybrid MIMO architecture for 6G and beyond," *IEEE Trans. Commun.*, vol. 74, no. 1, pp. 381–401, 2026.
- [79] R. W. Heath, Jr. *et al.*, "The tri-hybrid MIMO architecture," *IEEE Wireless Commun.*, pp. 1–7, 2026.